



universität
wien

MASTERARBEIT / MASTER'S THESIS

Titel der Masterarbeit / Title of the Master's Thesis

„ Synthesis and characterization of metal oxide clusters
attached to TiO₂ nanoparticles for photocatalytic
water splitting “

verfasst von / submitted by

Jasmin Sophia Schubert B.Sc

angestrebter akademischer Grad / in partial fulfilment of the requirements for the degree of
Master of Science (M.Sc)

Wien, 2018/ Vienna 2018

Studienkennzahl lt. Studienblatt /
degree programme code as it appears on
the student record sheet:

A 0660862

Studienrichtung lt. Studienblatt /
degree programme as it appears on
the student record sheet:

Chemie

Betreut von / Supervisor:

Univ.-Prof. Dr. Dominik Eder

Contents

List of Abbreviations	iii
Abstract	v
Zusammenfassung	vii
1 Introduction	1
1.1 Photocatalysis	3
1.1.1 Homogeneous vs heterogeneous photocatalysis	4
1.1.2 Photocatalytic water splitting	5
1.2 Photosynthesis as inspiration	7
1.3 Co-catalysts as strategy to tune photocatalytic performance	8
1.4 Synthetic strategies of nanoparticles	9
1.5 Our motivation	10
2 Characterization Methods	13
2.1 X-ray characterization methods	13
2.1.1 X-ray diffraction (XRD)	13
2.1.2 X-ray photoelectron spectroscopy (XPS)	14
2.2 Electron microscopy	16
2.2.1 Scanning electron microscopy (SEM)	16
2.2.2 Transmission electron microscopy (TEM)	17
2.3 Attenuated total reflectance Fourier transform infrared spectroscopy (ATR-FTIR)	18
2.4 Thermal gravimetric analysis (TGA)	19
3 Experimental	21
3.1 Synthesis of the metal oxide clusters attached to TiO ₂ -nanoparticles	21
3.2 Photocatalysis experiments	22
3.2.1 Reactor scheme	22
3.2.2 Experimental procedure	23

4	Results and discussion	25
4.1	Synthesis of the MO_x clustes on TiO_2 nanoparticles as substrate . .	25
4.1.1	Determination of the heat treatment procedure	27
4.2	Characterisation of the MO_x – TiO_2 composites	32
4.2.1	TEM analyses	32
4.2.2	TG analysis	37
4.2.3	XPS analyses	47
4.3	Photocatalytic water splitting experiments	53
5	Conclusions	57
	Acknowledgment	61
	Curriculum vitae	65
	References	65

List of Abbreviations

$\text{Co}(\text{acac})_3 - \text{TiO}_2$	$\text{Co}(\text{acac})_3$ attached on TiO_2
$\text{Co}(\text{acac})_3$	Cobalt (III) acetylacetonate
$\text{CoO}_x - \text{TiO}_2$	CoO_x attached on TiO_2
$\text{Cu}(\text{ac})_2 - \text{TiO}_2$	$\text{Cu}(\text{ac})_2$ attached on TiO_2
$\text{Cu}(\text{ac})_2$	Copper (II) acetate
$\text{CuO}_x - \text{TiO}_2$	CuO_x attached on TiO_2
$\text{Fe}(\text{acac})_3 - \text{TiO}_2$	$\text{Fe}(\text{acac})_3$ attached on TiO_2
$\text{Fe}(\text{acac})_3$	Iron (III) acetylacetonate
$\text{FeO}_x - \text{TiO}_2$	FeO_x attached on TiO_2
$\text{Mn}(\text{acac})_2 - \text{TiO}_2$	$\text{Mn}(\text{acac})_2$ attached on TiO_2
$\text{Mn}(\text{acac})_2$	Manganese(II) acetylacetonate
$\text{MnO}_x - \text{TiO}_2$	MnO_x attached on TiO_2
MO_x	Metall oxide
$\text{Ni}(\text{acac})_2 - \text{TiO}_2$	$\text{Ni}(\text{acac})_2$ attached on TiO_2
$\text{Ni}(\text{acac})_2$	Nickel (II) acetylacetonate
$\text{NiO}_x - \text{TiO}_2$	NiO_x attached on TiO_2
BSE	Backscattered electrons
EELS	Electron energy loss spectroscopy
EtOH	Ethanol

FTIR	Fourier transform infrared spectroscopy
HER	Hydrogen evolution reaction
MeOH	Methanol
NADP	Nicotinamide adenine dinucleotide phosphate
NHE	Standard hydrogen electrode
OEC	Oxygen evolving complex
OER	Oxygen evolution reaction
POM	Polyoxometalates
SE	Secondary electrons
SEM	Scanning electron microscopy
TEM	Transmission electron microscopy
TEOA	triethanolamine
TGA	Thermal gravimetric analysis
XPS	X-ray photoelectron spectroscopy
XRD	X-ray diffraction

Abstract

Photocatalysis is a promising way to convert and store light energy in a chemical bond by means of light-assisted catalytic processes, such as photocatalytic water splitting, which leads to the formation of H_2 . However, the limited implementation of photocatalysts for the H_2 generation is their inherent poor catalytic performance towards water splitting. This challenge is often addressed by the use of co-catalysts attached on the photocatalyst surface to improve the photocatalytic activity. The most commonly used co-catalysts today are noble metals, like Pt, for HER (hydrogen evolution reaction), and noble metal oxide, e.g. IrO_2 , for the OER (oxygen evolution reaction). But, noble metals are rare and expensive, thus development of novel not noble metals based co-catalysts is necessary. In this work we develop and investigate new photocatalytic systems with metal oxides as co-catalysts attached on TiO_2 nanoparticles. The chosen metals as co-catalyst are Mn, Co, Fe, Ni and Cu due to their excellent redox properties and their ability to accumulate, store and release charge, as demonstrated by biological processes of photosynthesis and hydrogen fixation. We focused on metal oxides due to their capacity to adopt various oxidation states without braking the structure. This property makes oxides suitable candidates to generate a self-recovering photocatalytic system acting as a charge transporting channel between the photocatalyst and the reactant.

In this work the co-catalytic nanoparticles have been synthesised *in situ* in the presence of TiO_2 nanoparticles by wet impregnation using Mn, Co, Ni and Fe acetylacetonates and Cu acetate salts followed by the generation of the corresponding oxides via post-calcination. Five slightly different synthetic methods have been selected for the impregnation due to instability of some precursors, and two different heat treatments have been applied to investigate the impact of the resulting co-catalyst composition on the performance.

The synthesised photocatalysts have been characterized by using SEM, TEM, EDX, XRD, XPS, ATR-FTIR, electron diffraction and TGA. The data revealed that the co-catalyst nanoparticles have been generated for all selected metals, although not homogeneously for all samples due to deficiencies of the synthetic protocol. We also conclude that various synthetic conditions and type of the metal precursor have a strong impact on the resulting morphology of the co-catalysts.

The composition of the co-catalyst nanoparticles was determined by XPS, as XRD and electron diffraction revealed an amorphous nature of the co-catalyst, thus making further characterisation with these methods impossible. However, complete characterisation with XPS was also not possible due to small co-catalyst concentration and charging of the samples, but it was possible to exclude certain metal species. This revealed that for the Mn, Co and Fe containing samples oxides have been generated (probably MnO, Mn₂O₃, CoO, Co(OH)₂ and FeO, respectively), while for the Ni and Cu samples beside the oxides also metallic species have been generated (probably NiO, Ni(OH)₂, Ni, Cu₂O and Cu, respectively).

The photocatalytic performance in HER has been tested for all the samples revealing NiO_x-TiO₂ and CuO_x-TiO₂ photocatalyst to be active towards H₂ generation, with the CuO_x-TiO₂ samples showing the highest activity. Our results show that samples calcined at lower temperature performed better compared to the ones treated at higher temperature, which can be related to that at higher temperatures the generated metallic species (probably the active HER species) get oxidized. On the other hand, the synthesised FeO_x-TiO₂, MnO_x-TiO₂ and CoO_x-TiO₂ composites exhibited no HER activity. These activity differences is probably related to the morphology (as NiO_x and CuO_x are coating the TiO₂) and the presence of metallic species in both NiO_x-TiO₂ and CuO_x-TiO₂ samples.

This study suggest the importance of the appropriate thermal treatment for the oxide generation, as well as the influence of the used metal and salt precursor, being all parameters affecting the resulting MO_x morphology, crystallinity and the type of the formed species, which consequently affect the photocatalytic performance. The synthesized composites can also be of interest to other photocatalytic processes such as water oxidation.

Zusammenfassung

Photokatalyse ist ein vielversprechender Weg, Lichtenergie durch lichtunterstützte katalytische Prozesse wie die photokatalytische Wasserspaltung in eine chemische Bindung umzuwandeln und zu speichern, was zur Bildung von H_2 führt. Jedoch ist die Implementierung von Photokatalysatoren begrenzt für die H_2 Erzeugung wegen ihrer inhärenten schlechten katalytischen Leistung für die Wasserspaltung. Diese Herausforderung wird oft durch den Einsatz von Co-Katalysatoren auf der Oberfläche des Photokatalysators gelöst, um die photokatalytische Aktivität zu verbessern. Die heute am häufigsten verwendeten Co-Katalysatoren sind Edelmetalle, wie Pt, für die Wasserstoff-Entwicklungsreaktion und Edelmetalloxid, z.B. IrO_2 , für die Sauerstoff-Entwicklungsreaktion. Aber Edelmetalle sind selten und teuer, daher ist die Entwicklung neuartiger, nicht edelmetallbasierter Co-Katalysatoren notwendig. In dieser Arbeit entwickeln und untersuchen wir neue photokatalytische Systeme mit Metalloxiden als Co-Katalysatoren auf TiO_2 Nanopartikeln. Die ausgewählten Metalle als Co-Katalysator sind Mn, Co, Fe, Ni und Cu aufgrund ihrer hervorragenden Redox-Eigenschaften und ihrer Fähigkeit, Ladung zu speichern und freizusetzen, wie biologische Prozesse der Photosynthese und Wasserstofffixierung zeigen. Wir haben uns auf Metalloxide konzentriert, da sie verschiedene Oxidationszustände annehmen können, ohne die Struktur zu verändern. Diese Eigenschaft macht Oxide zu geeigneten Kandidaten für die Erzeugung eines selbstregenerierenden photokatalytischen Systems, das als Ladungstransportkanal zwischen dem Photokatalysator und dem Reaktanten dient.

In dieser Arbeit wurden die Co-katalytischen Nanopartikel durch Nassimprägnierung mit Mn, Co, Ni und Fe Acetylacetonaten und Cu-Acetatsalzen und anschließender Erzeugung der entsprechenden Oxide durch Kalzinierung in situ synthetisiert. Fünf leicht unterschiedliche synthetische Methoden wurden für die Imprägnierung (aufgrund der Instabilität einiger Vorläufer) ausgewählt, und zwei verschiedene Wärmebehandlungen wurden angewandt, um den Einfluss der resultierenden Co-Katalysatorzusammensetzung auf die Leistung zu untersuchen.

Die synthetisierten Photokatalysatoren wurden mit REM, TEM, EDX, XRD, XPS, ATR-FTIR, Elektronenbeugung und TGA charakterisiert. Die Daten zeigten,

dass die Co-Katalysator-Nanopartikel für alle ausgewählten Metalle erzeugt wurden, wenn auch nicht für alle Proben homogen aufgrund von Mängeln des synthetischen Protokolls. Wir schlussfolgerten auch, dass verschiedene synthetische Konditionen und die Art des Metallvorläufers einen starken Einfluss auf die resultierende Morphologie der Co-Katalysatoren haben. Die Zusammensetzung der Co-Katalysator-Nanopartikel wurde durch XPS bestimmt, da XRD und Elektronenbeugung einen amorphen Charakter des Co-Katalysators zeigten und somit eine weitere Charakterisierung mit diesen Methoden nicht möglich war. Eine vollständige Charakterisierung mit XPS war aufgrund der geringen Co-Katalysator Konzentration und Aufladung der Proben nicht möglich, jedoch konnten bestimmte Metallspezies ausgeschlossen werden. Dies ergab, dass für die Mn, Co und Fe enthaltenden Proben Oxide erzeugt wurden (wahrscheinlich MnO , Mn_2O_3 , CoO , $\text{Co}(\text{OH})_2$ bzw. FeO), während für die Ni und Cu Proben neben den Oxiden auch metallische Spezies erzeugt wurden (wahrscheinlich NiO , $\text{Ni}(\text{OH})_2$, Ni , Cu_2O und Cu).

Die photokatalytische Leistung für die Wasserstoff-Entwicklungsreaktion wurde für alle Proben getestet, und zeigten das die $\text{NiO}_x\text{-TiO}_2$ und $\text{CuO}_x\text{-TiO}_2$ Photokatalysator aktiv sind, wobei die $\text{CuO}_x\text{-TiO}_2$ Proben die höchste Aktivität zeigen. Unsere Ergebnisse zeigen, dass Proben, die bei niedrigerer Temperatur kalziniert wurden, besser abschneiden als solche, die bei höherer Temperatur behandelt wurden, was damit zusammenhängen kann, dass bei höheren Temperaturen die erzeugten Metallspezies (wahrscheinlich die aktive Spezies) oxidiert werden. Andererseits zeigten die synthetisierten $\text{FeO}_x\text{-TiO}_2$, $\text{MnO}_x\text{-TiO}_2$ und $\text{CoO}_x\text{-TiO}_2$ Komposite keine Wasserstoff-Entwicklungsreaktion-Aktivität. Diese Aktivitätsunterschiede hängen wahrscheinlich mit der Morphologie (da NiO_x und CuO_x TiO_2 umhüllen) und dem Vorhandensein von metallischen Spezies in beiden $\text{NiO}_x\text{-TiO}_2$ und $\text{CuO}_x\text{-TiO}_2$ Proben zusammen.

Diese Studie zeigt die Bedeutung der angemessenen thermischen Behandlung für die Oxidbildung, sowie den Einfluss der verwendeten Metall- und Salzvorkörper, wobei alle Parameter die resultierende MO_x Morphologie, Kristallinität und die Art der gebildeten Spezies beeinflussen, die somit die photokatalytische Leistung beeinflussen. Die synthetisierten Komposite können auch für andere photokatalytische Prozesse wie die Wasseroxidation von Interesse sein.

Introduction

The 21st century is facing an environmental challenge against climate change and environmental pollution like human kind has never seen before. After the industrial revolution in the late 19th century the planet's surface temperature has increased by 1.1 °C.¹ Different catastrophic scenarios for the world were forecast if the global temperature raises up to 4 °C with more drought, hurricanes, melting of the poles, etc.² The responsible for this global warming, and so climate change, are the so called greenhouse gasses. These are molecules like CO₂, CH₄, N₂O, etc. Among these gases, the one with the most wide concern is CO₂. This gas, although being less active in greenhouse effect than CH₄, is produced on much greater scale compared to others, as the CO₂ emission to the atmosphere increased by 30 % since the industrial revolution, mainly due to the extensive combustion of fossil fuels. Thus, being the gas with the most important effect on climate change.

Every year the world population is growing, which implies a constantly increasing demand for energy supply.³ This leads to a growing consumption of fossil fuels resulting in a rapidly increasing CO₂ concentration in the atmosphere. To avoid the catastrophic consequences of those greenhouse gases there is a huge need for other, cleaner, greenhouse gasses free, sustainable energy sources.

Several renewable energy technologies are up to day available on the market. These include geothermal energy, hydropower, bioenergy, wind power and solar energy, among others.⁴ Geothermal energy is the thermal energy generated and stored in the earth lithosphere. However, its extraction can liberate trapped greenhouse gasses from the earth crust and is additionally related with high cost of the installation and instability of the earth surface. Hydropower uses the water flow to generate electricity. It is, however, limited to the area where enough water flow exist and has environmental consequences for the wild life. Bioenergy, such as biofuels, is a renewable energy source. However, its combustion still releases CO₂ as the main product. Wind power uses wind turbines to convert the wind flow into electricity. But wind is an intermittent source of energy and the turbines are expensive. Compared to all other renewable energy sources, solar energy is extremely abundant as 1.575–49.837 exajoules (EJ) per year is irradiated on the Earth. This

energy is way above the world energy consumption needs.⁵ And, at the end, it is the primary energy source for wind power and biofuel. But solar cells up to day are still expensive, not efficient enough and also an intermittent energy source as they can work only during the day. Thus, further investigation of those energy converting systems is needed.

The intermittent nature of many renewable energy sources implies a need for optimized energy storage systems.⁶ One promising candidate for energy storage is H_2 , as its energy content is much greater than that of other fuels such as of petrol, diesel, methanol, etc (table 1.1), reaching the unprecedented value energy density of 120 MJ kg^{-1} .^{7,8} Also, the H_2 combustion is pollutant and CO_2 free as it reacts with O_2 yielding H_2O as a product. This reaction is highly exothermic releasing a combustion heat of $1.4 \cdot 10^8 \text{ J kg}^{-1}$. Thus, this system stores a huge amount of energy in the chemical bond, making it a promising energy storage solution.

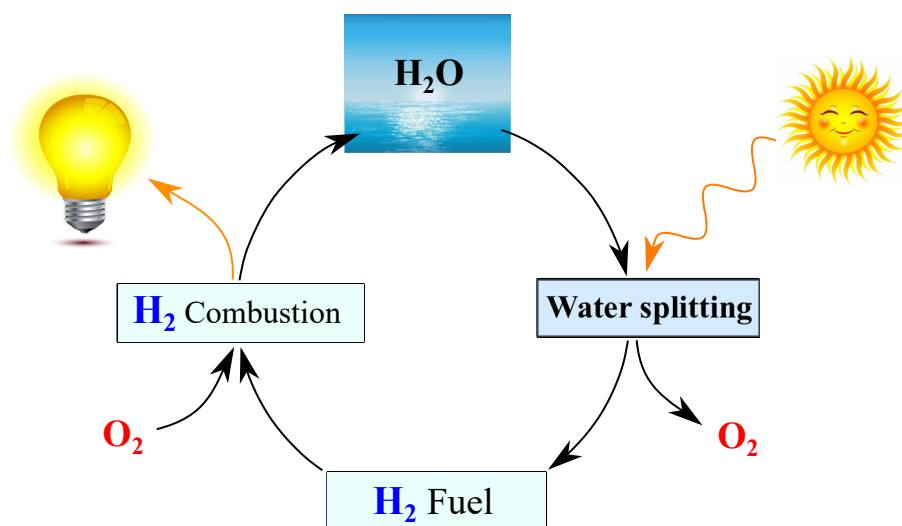


Figure 1.1: Scheme of the water splitting circle for the H_2 production.

The H_2 production up to day originates mainly from non renewable energy sources such as coal, oil and natural gas.⁹ H_2 generation from fossil fuel reaches 95 %, while from water (using electricity) and biomass it's only 4 % and 1%, respectively.¹⁰ As the combustion of fossil fuels (and so the H_2 production) are responsible for the greenhouse gasses generation, other H_2 sources have to be developed.

Water is a promising and clean H_2 production source as the water splitting process yields O_2 as the only side product. But, in order to induce this reaction an extensive amount of energy has to be invested. Today the main water splitting processes are electrolysis, photoelectrolysis, catalysis, photocatalysis, among others.

Table 1.1: Energy densities for different fuels.⁷

	Energy density	
	MJ kg ⁻¹	kWh kg ⁻¹
Hydrogen	120	33.3
Methanol	19.7	5.36
Petrol	42.0	11.36
Diesel	45.3	12.58
Kerosene	43.5	12.08

In electrolysis, the water molecule is cracked by applying an electric current, meaning that the H₂ production relies on previously generated electricity. As the required amount of energy to split water is very high, this method is uncompetitive with the H₂ production from coal and natural gas.⁷ A possible alternative is to use photoelectrochemical systems. Here, only a part of the required energy to split water comes from the externally applied voltage while the other part comes from the energy of light. In this case, for example, a photovoltaic system can be coupled with a photoelectrochemical cell. Pure catalyst, on the other hand, ideally only reduces the over potential needed for water splitting. Thus, the required amount of extra-energy to run the reaction is lowered. Photocatalysis is yet another alternative possibility. It can be considered to be an all-in-one system, where the water splitting and the light absorption takes place in the same material. In this manner, no need from external energy source to induce the reaction is needed. Hence, for all these reasons, this work has focused on the new synthesis of photocatalytic systems towards water splitting and H₂ generation, which will be further discussed in the next sections.

1.1 Photocatalysis

The word "photocatalysis" comes from the Greek word "*photo*", light, and "*catalysis*", substance that modifies the activation energy of a reaction, thus, affecting its kinetics. Hence, photocatalysis is a process where a reaction is accelerated through the absorption of light.

In 1972, Fujishima and Honda, were the first ones to use a stable semiconductor (TiO₂) for this application, which gave birth to the field of photocatalysis.^{11,12} A semiconductor is a solid state material with a band gap between the conduction band and the valence band (figure 1.2), thus, making it an insulator unless this band gap is overcome and free charge carriers are created.¹³ This valence band to conduction band transition can be provoked by using photons with an energy

above this band gap. By doing so the material absorbs the photon by exciting an electron to the conduction band and generating an electron-hole pair (exciton). The conduction band after the irradiation of the material with light gets populated with electrons, while the valence band with the corresponding holes. This means that reduction and oxidation reactions can take place at the conduction band and valence band, respectively. However, electrons want to be in the lowest energetic state. Thus, it has to be ensured that charge separation and effective extraction to the active sites takes place. In this manner, the reaction efficiency is limited by the exciton lifetime, the incident photon flux, the light absorption and the catalytic active sites of the material.

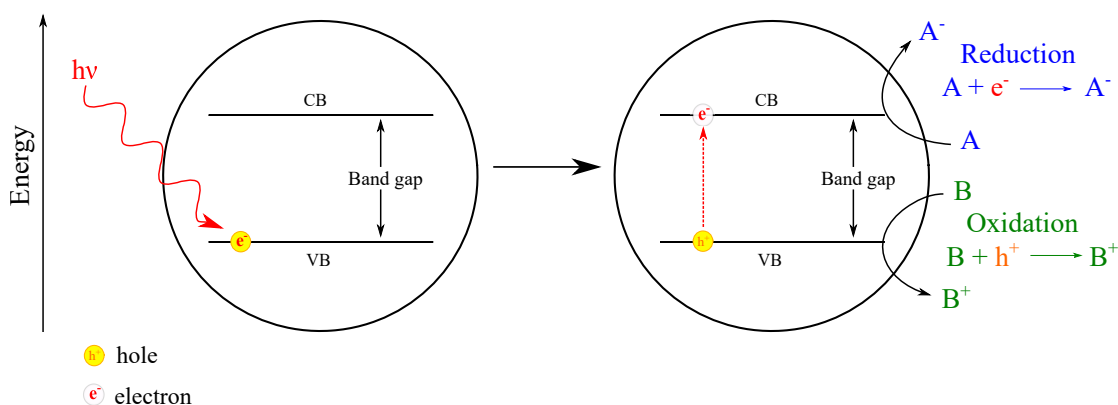


Figure 1.2: Representation of the photocatalysis mechanism. CB: conduction band and VC: valence band.

1.1.1 Homogeneous vs heterogeneous photocatalysis

Catalyst, and so photocatalyst, can be classified in two subgroups: homogeneous and heterogeneous catalysts. The homogeneous catalysis is when both, the catalyst and the reaction mixture, are in the same phase, for instance, both in liquid phase.¹⁴ While in heterogeneous catalysis the catalysts and the reaction medium are in different phases, e.g. the catalyst in the solid phase and the reaction mixture is a gas or liquid. Both kinds of catalysts present pros and cons.

A large number of different heterogeneous and homogeneous photocatalyst have been reported in literature.^{15–19} One of the main limitation to introduce the homogeneous catalyst in industry is its challenging recovery and stability. Recovery is an issue because both are in the same phase. Stability problems are due to degradation of the photocatalyst. Both points can be effectively addressed by using heterogeneous photocatalyst, like for instance oxides. They have inherent stability towards oxidation and recycling of the solid state particles can be accomplished

using various filters. Thus, finding so more application in industry. However, the homogeneous systems are easier to fine-tune by just changing the used ligands and or metal centres. A typical photocatalyst here are metal complexes and, more recently, POMs (polyoxometalates) .²⁰

1.1.2 Photocatalytic water splitting

The semiconductor material has to fulfill some condition in order to act as a photocatalyst and to be able to split water in O_2 and H_2 .^{11,16,21,22} Those condition are (i) the redox potential necessary to reduce water and generate H_2 has to be more negative for the semiconductor than the water reduction potential (0 V vs. NHE). Additionally, the oxidation potential has to be more positive than the water oxidation potential (1.23 V) (figure 1.3). (ii) The semiconductor has to be stable under the condition that the photocatalytic process takes place. i.e. against corrosion, decomposition, etc. (iii) The exciton lifetime has to be large enough that the photoreaction can take place, since if recombination dominates the energy will be released in form of heat or photons. (iv) The catalytic step is defined by surface character (presence of active sites) and the surface area (number of active sides) of the semiconductor, since the reactants (in this case water) needs to be adsorbed on the catalyst surface and induce the right reacting geometry. Also, the reactant-catalyst interaction has to be strong enough so that the adsorption takes place, but week enough that the products can leave the surface after it.

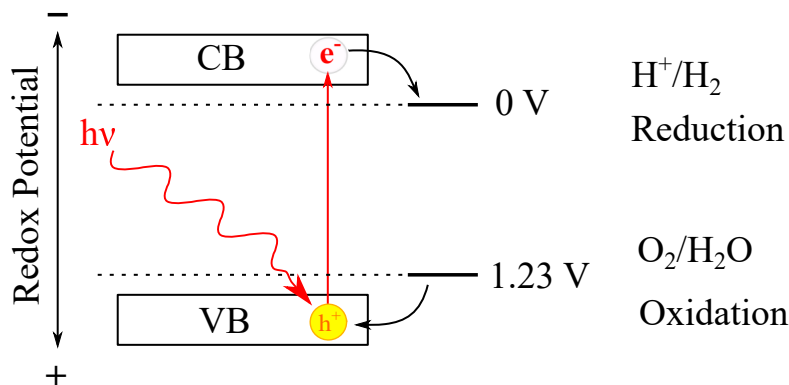


Figure 1.3: Scheme of a semiconductor band gap condition necessary for water splitting.

The water splitting process can be explained in three steps, shown in figure 1.4: (i) first absorption of the photon and the generation of an exciton takes place, as described before. (ii) in order for the photocatalytic reaction to take place, this electron-hole pair has to be efficiently separated to reach the photocatalyst surface. Once there (iii) the oxidation/reduction of water takes place on the corresponding photocatalytically active sites.

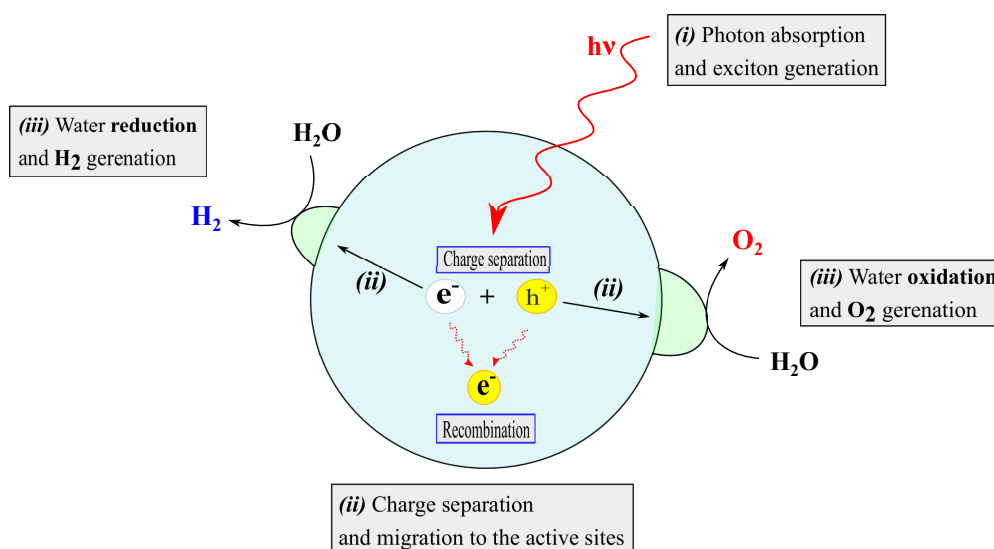


Figure 1.4: Photocatalytic water splitting steps.

1.1.2.1 TiO_2 as water splitting photocatalyst

Several possible semiconductor materials were studied in order to fulfil those conditions. Some of them are ZnO, CdS, ZnS, TiO_2 , among others.^{11, 12, 21, 23} Unfortunately non of them accomplish all those condition mentioned before to be an active and stable water splitting photocatalyst. Like for example, CdS has a suitable band position and band gap. But the generation of holes instead of oxidizing water, S^{2-} to S is oxidized, resulting in material degradation and destruction of the photocatalyst. ZnO also experiences this photocorrosion by reducing the O^{-2} to O_2 . TiO_2 on the other side is a non toxic, chemically stable and cheap photocatalyst with a high oxidizing power.^{11, 12, 16, 22, 23} But, unfortunately, it has two drawbacks.^{22, 23} First, it has a fast charge carrier recombination. The second, its band gap is in the UV light range (3.0 - 3.2 eV, rutile and anatase, respectively) of which just 5 % is in the solar spectrum that reaches the earth surface. In order to overcome those disadvantages doping, co-catalyst, etc were used.²²

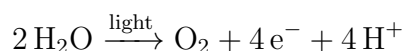
TiO_2 is found in nature in two crystalline forms, anatase and rutile. The photocatalytically more active one is anatase.^{11, 12, 16} However, it has been reported that a mixture of both phases enhances the photocatalytic activity. The reason is that the heterojunction between the two phases enhances the charge separation, and so the exciton lifetime. The usage of a co-catalyst can also improve this charge separation by extracting the charge carriers from the light absorber, which can lead to an enhanced photocatalytic activity. Also the usage of nanoscaled photocatalytic particles can improve the exciton life time, as the path length is shorter from the exciton generation to the active site. For those reasons this work

has concentrated on using TiO_2 nanoparticles (in the form of commercial P25 and anatase/rutile phase mixture) as a photocatalyst powder combined with novel co-catalysts to address the drawbacks of bare TiO_2 .

1.2 Photosynthesis as inspiration

Over million of years nature has learned how to store the light energy in chemical bonds with photosynthesis. As a general idea, it uses light to split water and store this energy in carbohydrates. With that the amount of energy stored by the photosynthesis yearly is about three times the global power consumption.²⁴

One of the main problems in photocatalysis and photovoltaic is the fast charge recombination that leads to a poor energy conversion. To overcome this problem photosynthesis uses an electron scavenger once the electron is excited by the chlorophyll in photosystem II.²⁵ This scavenger is pheophytin which then passes the electron to a quinone. This electron than is transferred to several proteins and molecules until reducing the proton to be stored in the form of NADPH nicotinamide adenine dinucleotide phosphate hydrate. However, the chlorophyll needs to recover this scavenged electron. This electron source is water, by a water splitting process carried out by a Mn cluster, called oxygen evolving complex (OEC) and with a overall reaction



where the H^+ are then reduced with ferredoxin NADP reductase.

The Mn cluster, which provokes the water oxidation, contains 4 Mn ions linked together by oxygens. The ferredoxin NADP reductase is a Fe containing protein, that provokes the reduction of the H^+ . In the electron transport from photosystem II to photosystem I, several other proteins and carrier molecules are used. Like plastocyanin and cytochrome which contains Cu atoms. This metals participate in many redox processes in biology since they can exist in various oxidation states. Also Co and Ni atoms have been found in proteins that participate in the hydrogen fixation in anaerobic bacteria,²⁵ thus metals that also participate in many redox reaction in nature.

Since the photosynthetic system shows to be a robust system, scientist since their discovery has the dream to replicate it.²⁶ Current research for artificial photosynthesis systems are to mimic enzymes like hydrogenases (proteins that either reduces or oxidises hydrogen).²⁷ Another system that many research groups try to re-create is a water oxidizing catalyst. Examples of artificial systems include some ruthenium complexes, or metal oxides like MnO_2 , Ni doped Co_3O_4 , Mn_2O_3 , among others^{28,29} for photocatalysis or photoelectrochemistry.

As nature has shown that Mn, Co, Fe, Ni and Cu are appropriated metals for water splitting/hydrogen fixation process (due to their redox properties), in this work we concentrate on these metals to develop novel co-catalysts for water splitting.

1.3 Co-catalysts as strategy to tune photocatalytic performance

In the previous section it was already mentioned the ability of co-catalysts to enhance the photocatalytic properties. The best known co-catalysts for the H₂ production is platinum as it presents high photocatalytic activity and stability.³⁰⁻³² But, it is rare and expensive, thus, limiting the industrial application by it. For those reasons research has continued to find a co-catalyst that is cheap, widely available in nature and stable.

Nickel has been reported in many publication for different systems to enhance the H₂ evolution reaction with respect to the pure TiO₂ substrate. Sreethawong et. al. reported the photocatalytic activity for H₂ evolution reaction by dispersing NiO on a mesoporous TiO₂ substrate.³³ In 1987 Kudo et.al used TiO₂ (anatase) nanoparticles and attached NiO on it.³⁴ They observed that in the NaOH solution the catalyst was able to decompose water, while in distilled water it was not working. Also, they reported by coating the sample with NaOH, the activity was dropped with respect to the pure NiO-TiO₂ photocatalyst in the NaOH solution. Lin et. al.³⁵ made a combination of NiO and CoO, revealing that the combination of both oxides enhances the activity. They claimed that this higher activity is a result of the improved charge separation of the electrons and holes by Ni and Co species, respectively. Another co-catalyst system reported with TiO₂ photocatalyst is Ni(OH)₂, where the activity compared to pure TiO₂ was enhanced 223 times by using MeOH³⁶ as sacrificial agent and 90 times by using TEOA (triethanolamine).³⁷ The enhancement was explained by electrons transfer from TiO₂ to Ni(OH)₂, as the later one has a higher redox potential. Authors suggest that by accepting electrons Ni²⁺ species get reduced and become metallic Ni active sites, thus, helping in both, charge separation and catalytic activation. Yan et. al.³⁶ compared the Ni(OH)₂ on TiO₂ to other metal oxides and hydroxides such as CoO_x, Co(OH)₂, NiO_x, Fe(OH)₃ and Cu(OH)₂ on the TiO₂ surface. The authors found that Ni(OH)₂ species resulted in the highest H₂ evolution activity. Tran et. al.³⁸ enhanced the TiO₂ performance by depositing Co²⁺ and Ni²⁺ species and reducing them to metallic Co and Ni. These TiO₂ nanoparticles coated with Co and Ni separately were compared with the traditional Pt co-catalyst, revealing to be only three times less active.

Other cobalt-based co-catalyst for HER have been reported by Si et. al.³⁹ using Co_3O_4 on TiO_2 nanosheets. Again, the authors suggest that upon illumination, Co species get reduced by the photoexcited electrons from TiO_2 to metallic Co species. This system showed to be comparable to the Pt co-catalyst presenting also high stability. Iron-based co-catalyst for TiO_2 has been also reported. Tada and co workers⁴⁰ attached FeO_x on TiO_2 . This system showed to increase the activity under visible light illumination, thus, affecting the required band gap energy for the electron-hole generation. Also Yu et. al⁴¹ reported this behaviour for TiO_2 photocatalyst under visible light. Here they used Fe(III) species grafted on TiO_2 which then induced an oxidative decomposition of 2-propanol. A similar behaviour has also been observed for Cu(II) attached on TiO_2 .⁴²

Copper has also widely been reported as an effective co-catalyst for TiO_2 . He and co workers⁴³ reported the use of $\text{Cu}_2(\text{OH})_2\text{CO}_3$ clusters as co-catalyst for HER from water splitting on mesoporous TiO_2 with comparable activities to the Pt co-catalyst. The authors suggest that the Cu^{2+} -containing clusters effectively extract photogenerated electrons, thus, enhancing the charge separation, while at the same time get reduced and yield metallic Cu, which then enables the HER releasing the electrons and getting re-oxidized. Also CuO attached on the TiO_2 surface revealed photocatalytic activity towards HER under sacrificial conditions.^{44,45}

While for all the mentioned metals some research has been done, for manganese in combination with TiO_2 for water splitting application this is not the case. One system containing MnO_x attached on a hollow sphere TiO_2 has been reported.⁴⁶ The authors used MnO_x for the OER and Pt for the HER generating a spatial separation of the two catalytic centres, as Pt was in the inside of the sphere and the MnO_x on the outer side.

Our literature overview shows that for Ni and Cu oxides several different systems have been reported in combination with TiO_2 . While for Fe, Co and Mn oxides this is not the case.

However, in other studies the water oxidation capacity of MnO_x has been reported in a combination with BiVO_4 as a photocatalyst. CoO_x has been highlighted as a promising system when deposited on other substrates like Ta_3N_5 , TaON etc.⁴⁷⁻⁴⁹ Also Fe-based co-catalyst have been reported to favour the OER. For the HER different photocatalytic substrates systems containing Ni species and/or Cu also have been reported. Thus, these metals show promising capacity to enhance the TiO_2 properties as a co-catalyst for water splitting.

1.4 Synthetic strategies of nanoparticles

The synthesis of nanoparticles can be done in two main ways: top-down and bottom-up. Meaning, generation of nanostructures by breaking down a bulky

system to nanoscale, or building up nanostructures from atoms or molecules.⁵⁰⁻⁵³

The generation and synthesis of nanoparticles can be approached by three main methods: mechanical, physical and chemical. The mechanical one is a top down approach, where mechanical milling, mechanical alloying, etc. is used to generate the nanostructures from bulk structures. The problem of those methods is that there is no control over agglomeration, contamination from the milling equipment, defects generation in the structures, etc. The physical methods are bottom up technique where to generate nanoparticles pulsed laser, or ion beam techniques, plasma synthesis, etc. can be used. These methods, however, need special and often costly equipments. The third method is the chemical route. This method include sol-gel processes, hydrothermal synthesis, microemulsions, colloidal solution, wet impregnation, etc. In the sol-gel technique the precursor salt is solubilized in a solvent, then a reagent is added to surround the colloids and stabilize them. For the generation of oxide structures the sol gets hydrolysed and then undergoes condensation. Then by precipitation uniform nanoparticles can be generated. This method allows the generation of highly homogeneous nano samples, and control of the purity, morphology and composition. But this requires high cost of the reactants. In the hydrothermal route high temperature and high pressures are used to generate the nanostructures. In colloidal solution the nanoparticles are stabilized by the use of surfactants, thus, providing a fine control over the size and morphology. But again the use of capping agents increases the costs and number of steps in the synthesis and may result in undesired side reactions and contamination. In wet impregnation the nanoparticles are generated through precipitation. The solvent is evaporated generating a constant supersaturation of the solution, thus, resulting in constant precipitation of the solid state material. If the conditions are rightly chosen, nanoparticles can be generated in this way. This technique has the advantage to use less reactants for the generation of particles, and so it became a cheap and simple route for nanoparticles synthesis, although, paying the prize of less control of the morphology and size.

1.5 Our motivation

The renewable energy source systems up to day are not mature enough to cover the world energy needs. As a result the main energy production still comes from non clean and non renewable sources. Also the storage of energy produced in excess is still in its infancy. Since energy consumption is growing and growing by every year, there is a urgent need to perfectionate the production as well as the storage of clean and renewable energy. One suitable candidate for clean energy storage is H_2 as the chemical bond contains high energy density. But its main production is still from gas, petrol, etc. For those reasons in this thesis we investigated alternative

ways for photocatalytic H₂ production through water splitting. In this process the sunlight is used to break the water molecule in H₂ and O₂, thus, giving access to clean energy source were the only "waste" product is O₂.

Much research has been done up to day on H₂ production through water splitting, and specially with TiO₂ after Fujishima and Hondas discovery for its photocatalytic activity in 1972. The reason for the vivid interest in using TiO₂ for this application are its unique properties. TiO₂ is chemically stable against acid/base/ilumination conditions, shows no toxicity, is cheap and widely available, with a suitable band gap for water splitting and highly oxidizing power. This inherent properties makes TiO₂ a superior candidate as a water splitting photocatalyst. But, TiO₂ showed to have several drawbacks to be an efficient water splitting photocatalyst. One of those hindrance is that it has a fast electron hole recombination as also poor catalytic active sites on its surface. To overcome those limitations a possible strategy is the use of co-catalysts. This enhances the electron-hole life time as charge separation is achieved by the co-catalyst as a charge scavenger. In addition, it enhances the performance by generating new catalytic active sites. In this ways TiO₂ is used as a light antenna and the co-catalyst as the catalytically active part.

In spite of the broad research done in this field, not much has been accomplished in using metal oxides as co-catalysts for water splitting. The use of metal oxides have several advantages as they have the capacity to adopt different oxidation states as well as to be more stable towards degradation. For those reasons in this thesis we focused on the use of metal oxides as co-catalyst. The most efficient and widely used co-catalyst for the reduction of water is platinum, an expensive and rare metal. While for the oxidation reaction of water it is IrO₂, or RuO, also rare and expensive. To archive large scale industrial application the used raw materials have to be cheap, widely available and the photocatalyst has to be recyclable and efficient. Nickel, manganese, cobalt, iron and copper are extensive used metals in many different systems for redox application by industry, research and nature. The reason for it, is their excellent redox properties, as they can exist in several different oxidation states (condition necessary to generate a self recovering photocatalytic system) and also their availability. For all those reasons, in this thesis a innovative photocatalytic system is investigated with Mn, Co, Fe, Ni and Cu metal oxides as co-catalysts immobilized on TiO₂ nanoparticles.

Characterization Methods

2.1 X-ray characterization methods

The characterization and determination of the chemical composition and crystal structure of materials are of great interest for the scientific community and industry. X-rays are high energetic electromagnetic radiation with a wavelength, λ , ranging between 0,01 and 10 nm.⁵⁴ These unique property makes it suitable to obtain information at the atomic scale as the interatomic spacing lies in the same order of magnitude.

When an X-ray beam interacts with matter two processes occur: absorption of an X-ray photon causing the expulsion of an electron and scattering of the incident beam, phenomena used in X-ray photoelectron spectroscopy (XPS) and X-Ray diffraction (XRD), respectively.

2.1.1 X-ray diffraction (XRD)

In an ordered crystal system the atoms present a regular arrangement with an associated ordered electron density. When the incoming X-ray radiation interacts with the electrically charged electron density, scattering occurs. The determination of the inter-planar spacing, d , of the atoms provides information about the crystal parameters. These values can be determined via the Bragg law of diffraction

$$2 d \sin\theta = n \lambda, \quad (2.1)$$

where d is the inter-planar spacing, θ the scattering angle of the incident beam to the atomic plane, n a positive integer and λ the wavelength of the incoming beam. To obtain a good resolved Bragg peak and to minimize the background signal and peak broadening it is crucial to work with a monochromatic light.

To have constructive interference of the scattered beams, condition necessary to obtain a diffractogram, the path length difference of the scattered beams has to fulfil the Bragg condition $2 d \sin\theta$ (figure 2.1). Otherwise, destructive interference takes place and lower intensities or no signal is observed.

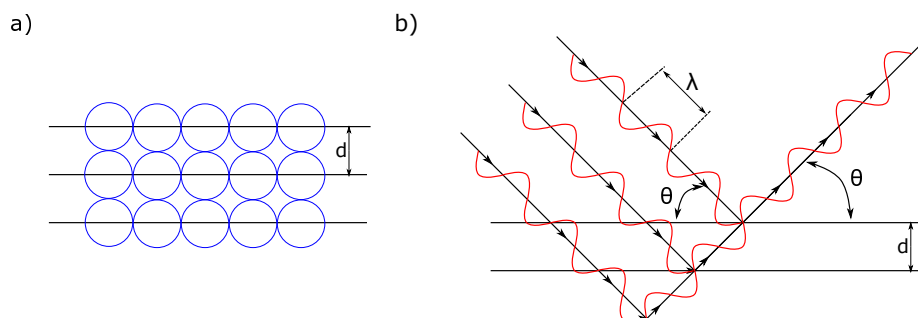


Figure 2.1: a) planes of ordered arrangement of atoms b) X-ray diffraction with a path length difference between the different layers generating constructive interferences (Bragg diffraction).

In this work for the in-situ experiments an XPERT III: PANalytical XPert Pro MPD (Θ - Θ Diffractometer) was used. The sample was placed on a sample holder and irradiated with a Cu X-ray source. The signal was acquired with Bragg-Brentano Θ / Θ -diffractometer geometry ranging from 5° to 80° degrees. The detector system was a semiconductor X'Celerator (2.1°) detector. The obtained diffractogram was plotted in intensity (a.u) vs 2θ (degrees). The experiment was performed under air flow and temperatures ranging from 25°C to 800°C .

For the ex-situ experiments a XPERT II: PANalytical XPert Pro MPD (Θ - Θ Diffractometer) was used. The sample was irradiated with a Cu X-ray source on a sample holder. The signal was obtained with a Bragg-Brentano Θ / Θ -diffractometer geometry from 10° to 80° degrees. A X'Celerator (2.1°) detector was used to collect the data. The diffractogram was plotted in intensity (a.u) vs 2θ (degrees). The experiment was performed under air flow.

2.1.2 X-ray photoelectron spectroscopy (XPS)

X-ray photoelectron spectroscopy is a powerful method to determine the chemical composition and electronic state of the elements within the first 10 nm of the surface and down to a concentration of a part per thousand.⁵⁵ In these method the X-ray beam is absorbed by the valence electrons which gain kinetic energy and escape the atomic orbital. If enough kinetic energy is gained, these electrons escape the surface of the material and reach the detector (figure 2.2). Thus, electrons coming from the bulk of the material do not contribute to the measured signal as they are absorbed by inelastic collision with neighbouring atoms. Hence, only the electrons from the outer surface will reach the detector and form part of the spectra. Due to the aforementioned collision high vacuum or ultra high vacuum is required.

The measured magnitude is the kinetic energy of the expelled electrons. How-

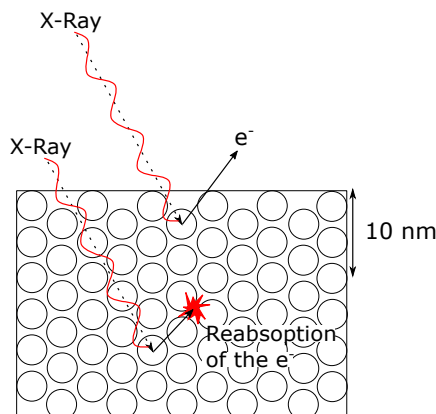


Figure 2.2: Schematic representation of the absorption of the x-ray by the materials atoms. These gain kinetic energy and escape the surface or are reabsorbed by the inelastic collision with the other atoms in the bulk of the material. The electrons able to escape the surface of the material are in between the first 10 nm of the surface of the bulk material.

ever, this depends on the incident x-ray photon energy. Thus, the represented magnitude in the spectrum is the bonding energy of the electron to the atom vs intensity. These parameters are related through the Einstein equation

$$E_{\text{bonding}} = E_{\text{photon}} - (E_{\text{kinetic}} + \phi), \quad (2.2)$$

where the E_{bonding} corresponds to the bonding energy, E_{photon} the energy of the x-ray photons, E_{kinetic} to the electron kinetic energy and ϕ the work function of the instrument detector.

In these research all measurements were carried out on a custom built SPECS XPS-spectrometer equipped with a monochromatised Al-K α X-ray source (μ 350) and a hemispherical WAL-150 analyser (acceptance angle: 60°). All samples were mounted onto the sample holder using double-sided carbon tape. Pass energies of 100 eV and 30 eV and energy resolutions of 1 eV and 100 meV were used for survey and detail spectra respectively (excitation energy: 1486.6 eV, beam energy and spot size: 70 W onto $400 \mu\text{m}$, angle: 51° to sample surface normal, base pressure: 5×10^{-10} mbar, pressure during measurements: 2×10^{-9} mbar). To reduce charging effects a broad-spot low energy electron source (SPECS FG 22 flood gun) was used for charge compensation (8-12 eV/15-30 μA) in some samples (containing Cu, Mn, Fe). Data analysis was performed using CASA XPS software, employing transmission corrections (as per the instrument vendor's specifications), Shirley/Tougaard backgrounds and Scofield sensitivity factors. Charge correction was applied so the adventitious carbon peak (C-C peak) was shifted to 284.8 binding energy (BE). All content values shown are in units of relative atomic percent (at%), where the

detection limit in survey measurements usually lies around 0.1-1 at%, depending on the element. The accuracy of XPS measurements is around 10-20% of the values shown. Assignment of different components was primarily done using Refs.

2.2 Electron microscopy

Electron microscopy uses electrons to generate an image, as photons do in optical microscopes. Electrons, similarly to photons, can be described as particles or waves. Thus, they can be used to generate an image, the same way than visible light does i.e. photons.

The advantage of an electron microscope compared to a light microscope is its higher resolving power. The wavelength used to generate an image in the visible range is 400 - 700 nm, with a resolution limit of 200 nm due to diffraction.⁵⁶ Electrons, on the other hand, can archive wavelength (useful in microscopy) up to 0,001 - 0,01 nm. Thus, electrons can reveal morphological features down to the atomic level.

Different kind of electron microscopes exist today, the most used ones are scanning electron microscopy (SEM) and transmission electron microscopy (TEM). As the name suggest, the difference between the two methods is that SEM works in a scanning mode, while TEM works in a transmission mode. Thus, different information can be extracted.

2.2.1 Scanning electron microscopy (SEM)

The scanning electron microscope uses a focused electron beam with an acceleration voltage between 1 keV and 30 keV.⁵⁶ These highly energetic electrons loose their energy by interacting with the sample and in this way provide so different information depending which phenomena are measured. The recorded signal is composed of secondary electrons (SE) , backscattered electrons (BSE) , X-rays, cathodoluminescence and auger electrons (figure 2.3). SE and BSE are used to generate the image, where the first ones are excited electrons from the sample escaping the surface. Hence, supplying morphological and topological information. The latter are electrons scattered back from the surface. Thus, atoms with higher electron density scatter the incoming electrons more strongly and so appear brighter than the lighter elements. Consequently, they provide information of different phases. X-Rays are generated by inelastic collision of the electron beam with the electrons of the inner atomic shell of the sample. Thus, elemental composition can be determined with these characteristic X-rays.

In our study a FEI Quanta 250 FEG at 200 V was used

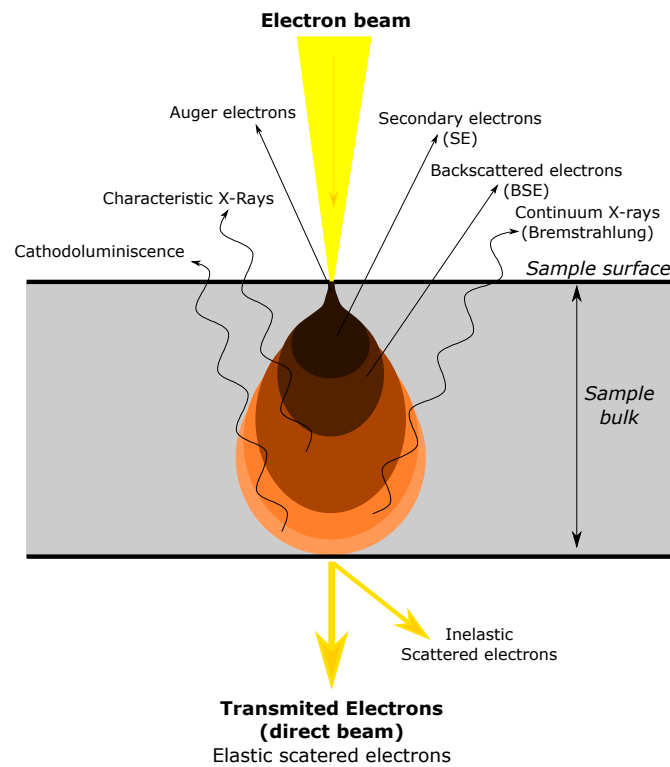


Figure 2.3: Figure representing the different interaction of the incoming electron beam with the sample. Each signal comes from a different thickness of the sample, obtaining so information of the different layers. It is also represented the transmission mode used in TEM.

2.2.1.1 Electron dispersive X-rays spectroscopy (EDX)

EDX is a technique used for elemental analysis of a sample. The used signal here are the characteristic X-rays that are generated when an electron from a higher energetic orbital jumps to a lower energetic one. To produce this transition an excitation source has to be used to first eject the electron from the inner shell by inelastic collision, like highly energetic electrons. The excess of energy from these transition is released in form of characteristic X-rays corresponding to a certain transition and element. Hereby, the chemical composition can be determined.

2.2.2 Transmission electron microscopy (TEM)

The transmission electron microscope, in contrast to SEM, works in a transmission mode (figure 2.3) with a beam energy ranging 100 - 400 keV.⁵⁷ The sample thickness have to be in the range of 100 nm, or suspended on a grid,⁵⁶ in order for the electrons to be able to cross through the sample and being detected by the detector.

When electrons pass through the sample they get unscattered (direct beam) or scattered with different angles by the sample depending on the chemical composition and thickness of the specimen. The higher is the electron density in the sample, the more scattering takes place. Hereby, the image contrast of the different regions of the sample is generated. Thus, different phases, defects, atomic composition, etc can be detected. Due to these wave properties of the electron, also diffraction patterns can be recorded of the specimen, like with X-rays, and by that crystal structure parameters can be determined. Due to the electric charge of the electrons they are scattered more strongly than X-rays, which leads to much higher intensities and shorter exposure times.

In these work a FEI TECNAI F20 at 200 kV was used.

2.2.2.1 Electron energy loss spectroscopy (EELS)

Electron energy loss spectroscopy is an analysis technique used to determine bonding energy, oxidation state of the atoms, band gaps (if present), dielectric response, specimen thickness and electron density.⁵⁷

The technique relies on the determination of the kinetic energy distribution of the electrons coming out of the sample. This means, when an electron beam passes through the specimen, these can be scattered in an elastic or inelastic way. With other words, electrons that passed through the sample maintaining their kinetic energy and electrons losing certain amount of kinetic energy, due to coulombic interaction with the atoms.

The spectra are represented in energy loss (eV) vs the intensity. These are separated in two regions providing different kind of information. The low-loss regime (below ~ 50 eV) and the high-loss region. These correspond to the plasmon excitation and to the ionization of the atoms, respectively.

In these work a FEI TECNAI F20 at 200 kV was used.

2.3 Attenuated total reflectance Fourier transform infrared spectroscopy (ATR-FTIR)

Infrared spectroscopy is a technique that exploits the fact that molecular boundaries can absorb certain frequencies of electromagnetic waves. The absorption occurs at the resonant frequency, i.e the absorbed frequency matches the vibrational frequency of the boundary. These resonant frequencies are in the infrared range.

By determining the absorbed amount of energy, it can be deduced which kind of characteristic chemical bonds are present in the molecule. Thus, to determine which frequencies are absorbed the sample has to be scanned at each wavelength

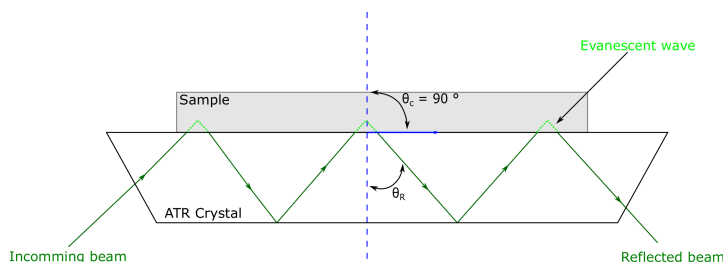


Figure 2.4: Schematic of an ATR system. The incoming IR beam is reflected with an angle θ_R , and generates an evanescent wave at the interface. The blue dashed line represents the normal direction to the surface and the blue arrow the direction where total reflectance takes place, i.e. at 90° from the normal.

and this is time consuming. So, in Fourier transform IR (FTIR) instead of scanning the sample with different monochromatic wavelength, this is done by shining a beam containing different wavelength at once.⁵⁸ The data then is treated by Fourier transform and a spectrum is obtained.

Attenuated total reflectance (ATR) is a FTIR sampling method, that enables to measure the sample directly in the solid or liquid state without further treatment. The phenomenon used here is the total internal reflection which generates an evanescent field in the measured sample (figure 2.4). Two conditions are needed in order for the total internal reflection to take place.⁵⁹ The incident beam must be reflected at an angle equal or greater than the critical angle, θ_c , and the refractive index of the crystal must be much greater than that of the sample. When these conditions are fulfilled an evanescent field is generated. It penetrates generally few microns ($0.5 \mu\text{m} - 5 \mu\text{m}$) into the measured sample, depending on the wavelength, the refractive index of the crystal and the angle of the incident beam.⁵⁸ The evanescent field is attenuated for the energies in which the sample absorption is high. These attenuation yields information about the nature of the chemical bonds present in the sample. The used crystal materials for the total reflectance, due to their high refractive index, are zinc selenide (ZnSe), germanium (Ge), thallium-iodide (KRS-5) or diamond.

In this work a PerkinElmer FT-IR Spectral UATR-TWO with a spectrum Two Universal ATR (Single Reflection Diamond) accessory was used.

2.4 Thermal gravimetric analysis (TGA)

Thermal gravimetric analysis (TGA) is a technique to determine the mass change of a sample at different temperatures or time.⁶⁰ This experimental technique is used to determine the decomposition of a sample by losing the crystalline water,

volatile constituents in the sample, the desorption and adsorption of gasses on the specimen, etc. Also the oxidation of metals under air and reduction of substances can be followed by using different gas environments. All these can be determined by plotting the mass % vs time or temperature.

The experiment can be performed in different ways depending on the information that needs to be extracted. So, the sample can be heated up at a constant rate (dynamic measurement), or hold at a constant temperature (isothermal measurements) or also non-linear measurement can be set up where the parameters are specifically adjusted. To perform the measurements a crucible is used, generally made of aluminium oxide, to hold the sample. This is connected to a precision balance that measures the weight change during the experiment.

In this work a PerkinElmer Thermogravimetric Analyser TGA 8000 was used. With a dynamic method at a heating rate of 5 °C/min under air heated from 25 °C to 800 °C and a Al₂O₃ crucible.

Experimental

3.1 Synthesis of the metal oxide clusters attached to TiO₂-nanoparticles

The synthesis of the metal oxide cluster attached on TiO₂ was performed through a wet impregnation synthetic route using five different environments. In water under ambient atmosphere, water under N₂ atmosphere, EtOH under ambient atmosphere, EtOH under N₂ atmosphere and EtOH under vacuum. The used precursors were Mn(acac)₂, Co(acac)₃, Ni(acac)₂, Fe(acac)₃ and Cu(ac)₂ to generate the corresponding metal oxide (figure 3.1). Where the anion acac corresponds to acetylacetonate and ac to acetate. The TiO₂ nanoparticles were commercially obtained from Degussa (P25).

The general synthesis procedure used for all samples was dissolving TiO₂ (400 mg, 5 mmol) in 20 ml of the corresponding solvent, except for the Fe(acac)₃ in H₂O sample, which was 40 ml, due to limited solubility. The suspension was stirred for some minutes and the precursor was added. Then, the solution was subjected to sonication to assist salt dissolution and homogenisation of the suspension components. The resulting mixture was left stirring at 60 °C until total evaporation of the solvent and then dried at 80 °C in the oven for 5h. For the samples prepared in vacuum, no additional heating was applied. Afterwards, the samples were heat treated at different temperatures in a muffle oven to generate the corresponding ox-

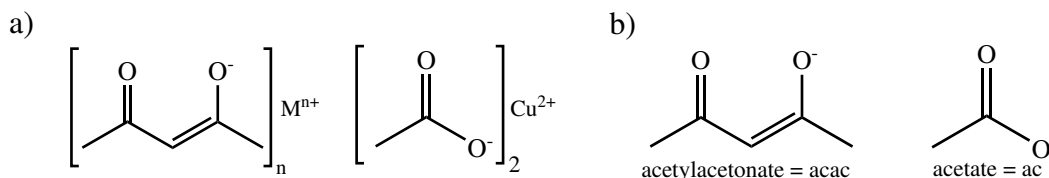


Figure 3.1: a) General formula for the metal acetylacetonate and acetate salts. M = Mn, Co, Ni or Fe. b) Representation of the chemical structure of the anions.

ides. The chosen heat treatment temperatures and the amount used of precursors are summarized in Table 3.1.

The used amount of each metal salt for the experiments (figure 3.1) were taken with the assumption of each metal oxide with a cluster size of 1.5 nm and a 10 % coverage of the TiO₂ nanoparticles. The surface of TiO₂ is about 55 m⁻²/g.⁶¹

Table 3.1: Used amount for the synthesis of precursors in mmol, mg and the corresponding heat treatment for each sample.

	Used amount		Heat treatment	
	mmol	mg	°C	Time (h)
Mn(acac) ₂	0.248	62.7	350	10
			270	3
Co(acac) ₃ · 2 H ₂ O	0.294	75.6	350	10
			230	3
Ni(acac) ₂ · 2 H ₂ O	0.113	29.1	350	10
			300	3
Fe(acac) ₃	0.26	92	350	10
			270	3
Cu(ac) ₂ · 2 H ₂ O	0.326	59.2	350	10
			270	3

3.2 Photocatalysis experiments

3.2.1 Reactor scheme

The photocatalytic experiments were performed in a glass reactor with a quartz cap transparent to the UV light (see figure 3.2). The reactor was equipped with a argon gas in and outlet to the reaction volume to constantly purge the system to deliver the gaseous reaction products to the detector. The reaction medium was surrounded by a water cooling system to control the temperature and to condense the water/MeOH back in to the reactor. Further, a CaCl₂ trap was used before the gas reached the X-Steam Emerson gas detector and the Agilent Micro gas chromatograph (GC) to remove the rest of water/MeOH that was not condensed back by the cooling system. The argon flow was controlled with a mass flow controller (MFC) installed before the argon gas reached the tank. The UV lamp was placed on the top of the reactor, on the quartz cap. The used light source was a SOLIS LED 365 nm lamp.

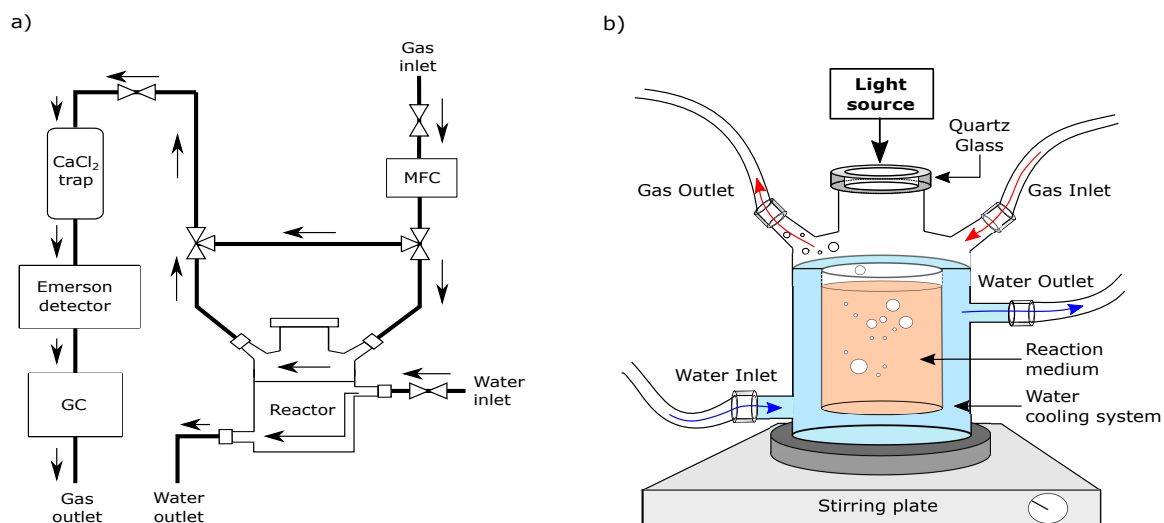


Figure 3.2: a) Photocatalytic set-up scheme of the gas and water flow through the reactor. b) Detailed representation of the photocatalytic gas evolution Reactor.

3.2.2 Experimental procedure

In the photocatalysis experiment 10 mg of catalyst was dissolved in 25 ml of water and 25 ml of MeOH. This solution was stirred and argon was bubbled for 5 minutes through the solution, to purge all the air dissolved. Then the reactor was closed and after 5 minutes the argon flow was change from 100 ml/min to 30 ml/min and the Emerson detection was started. After 30 minutes of stabilization of the signal the UV lamp was switched on. After 15 minutes the lamp was switched off.

Results and discussion

4.1 Synthesis of the MO_x clusters on TiO_2 nanoparticles as substrate

The synthesis of the MO_x clusters on TiO_2 nanoparticles as substrate ($\text{MO}_x - \text{TiO}_2$) was made using different synthetic routes, since the morphology and structure, and so their functionality, depends on how it was synthesised.⁶²⁻⁶⁴ The first synthesised $\text{MO}_x - \text{TiO}_2$ composite was dissolving the $\text{Mn}(\text{acac})_2$ salt with TiO_2 . The used method was to dissolve TiO_2 and the Mn salt in water and left stirring until complete evaporation of the solvent at 60 °C. This was done with a reference experiment only containing the salt, to determine if changes are observable under this condition. This showed that the reference solution changed the colour from brown to black few minutes after the heating was turned on. The cause of this apparent instability with temperature of the $\text{Mn}(\text{acac})_2$ can have several reasons. One of them is that Mn most stable oxidation state is Mn^{3+} instead of Mn^{2+} , oxidation state in the used Mn precursor salt for the deposition. Thus, in water, and oxidative milieu, it gets oxidized. The other possibility for the colour change is that it generates a complex with water.

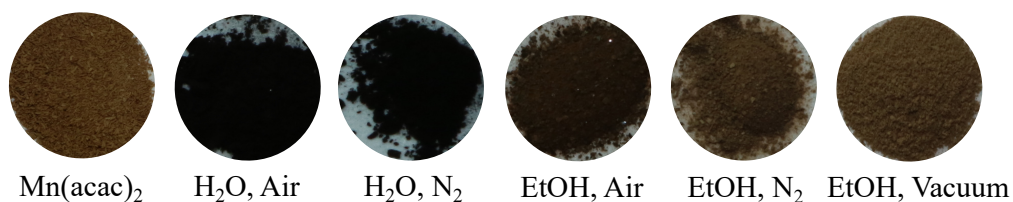


Figure 4.1: Pictures of the $\text{Mn}(\text{acac})_2$ before and after each synthetic method.

Due to this instability of the Mn salt other conditions were tried with the idea to avoid oxidation (by atmospheric oxygen) or water-based effects. The first one was to bubble N_2 through the water solution, to scavenge the dissolved O_2 . The second one was to use EtOH instead of water. The third one was EtOH with N_2



Figure 4.2: Photos of the composite samples obtained with the different synthesis methods.

bubbling through the solution to avoid both effects of water and O₂. The fourth, and last, method was using EtOH at vacuum, without applying heat, to avoid also kinetic effects. In figure 4.1 it is shown the Mn salt reference experiments after the different synthetic routes. The samples generated in water turned black while the ones dissolved in EtOH kept the original brown colour. Also it is noticeable that the vacuum treated sample slightly changed the colour to lighter brown. This results suggest that the main responsible for the change in colour for the Mn precursors is water. Hence, a possible water complex is generated under this conditions. A reason for the vacuum sample small change in colour could be because the O₂ was removed completely from the solution under this condition. Thus, no oxidative

agent was present in the solution. Meaning, that probably also O_2 has an effect by possibly oxidizing the Mn^{+2} . The other difference is that no heat was used for the evaporation of the solvent. So, any kinetic effect of reaction is avoided leading to less side reactions of the precursor.

The $Mn(acac)_2 - TiO_2$ composite, with $Mn(acac)_2$ adsorbed on the TiO_2 substrate, also showed this colour change like the pure precursor salt in water, EtOH and vacuum (figure 4.2). Due to the strong influence of the synthetic environment on the resulting colour - and, consequently, on the morphology and structure of the resulting composites - all five synthetic routes were used for the rest of the metal salts to so generate the $Co(acac)_3 - TiO_2$, $Ni(acac)_2 - TiO_2$, $Fe(acac)_3 - TiO_2$ and $Cu(ac)_2 - TiO_2$ composites.

Figure 4.2 shows also the other composites. There it is observable that for the $Co(acac)_3 - TiO_2$ also a slight change in colour from the water, EtOH and vacuum sample is appreciable. While for $Ni(acac)_2 - TiO_2$ all samples look the same. For $Fe(acac)_3 - TiO_2$ the vacuum sample shows a lighter colour while the water and EtOH samples present a change in the grain structure but not in colour. The $Cu(ac)_2 - TiO_2$ sample shows also the same behaviour as $Co(acac)_3 - TiO_2$. The reason for the lower degree of observable colour change in these samples is that the salt precursors used for these syntheses contain metal ions in their most stable oxidation state: Co^{3+} , Fe^{3+} , Cu^{2+} and Ni^{2+} . Thus, no oxidation of the metals will be expected in these mild condition. A possible reason for the small change in colour and grain in these samples is that the different solvent and the presence of O_2 and N_2 induces different structures and bondings between the metal salts and the TiO_2 . Also it will have an effect in the generated metal oxide species on the TiO_2 the different synthesis. Thus, affecting the observed morphology and colour.

4.1.1 Determination of the heat treatment procedure

The corresponding metal oxide clusters on the TiO_2 were generated via thermal decomposition. To determine the optimal heat treatment TGA, in-situ XRD and ex-situ ATR-FTIR at different temperatures of the pure precursors (figure 4.3) was performed as well as a TGA of the composites (figure 4.6).

The TGA of $Mn(acac)_2$ shown in figure 4.3a revealed that the thermal decomposition of the pure salt start at 148 °C and ends at 353 °C. The kink observable at 254 °C corresponds to the decomposition of the first acetylacetonate and the second step to the decomposition of the second one. Leading to the formation of a Mn_3O_4 and Mn_2O_3 mixture. The formation of these oxides was confirmed by XRD analysis in figure 4.3a where it is demonstrated that the precursor is stable until 150 °C. Then, from 200 °C Mn_3O_4 is formed and from 650 °C the formation of Mn_2O_3 is visible in the XRD diffractogram. These is also confirmed by the ATR-FTIR spectra where after 270 °C no organic residue is observed and the

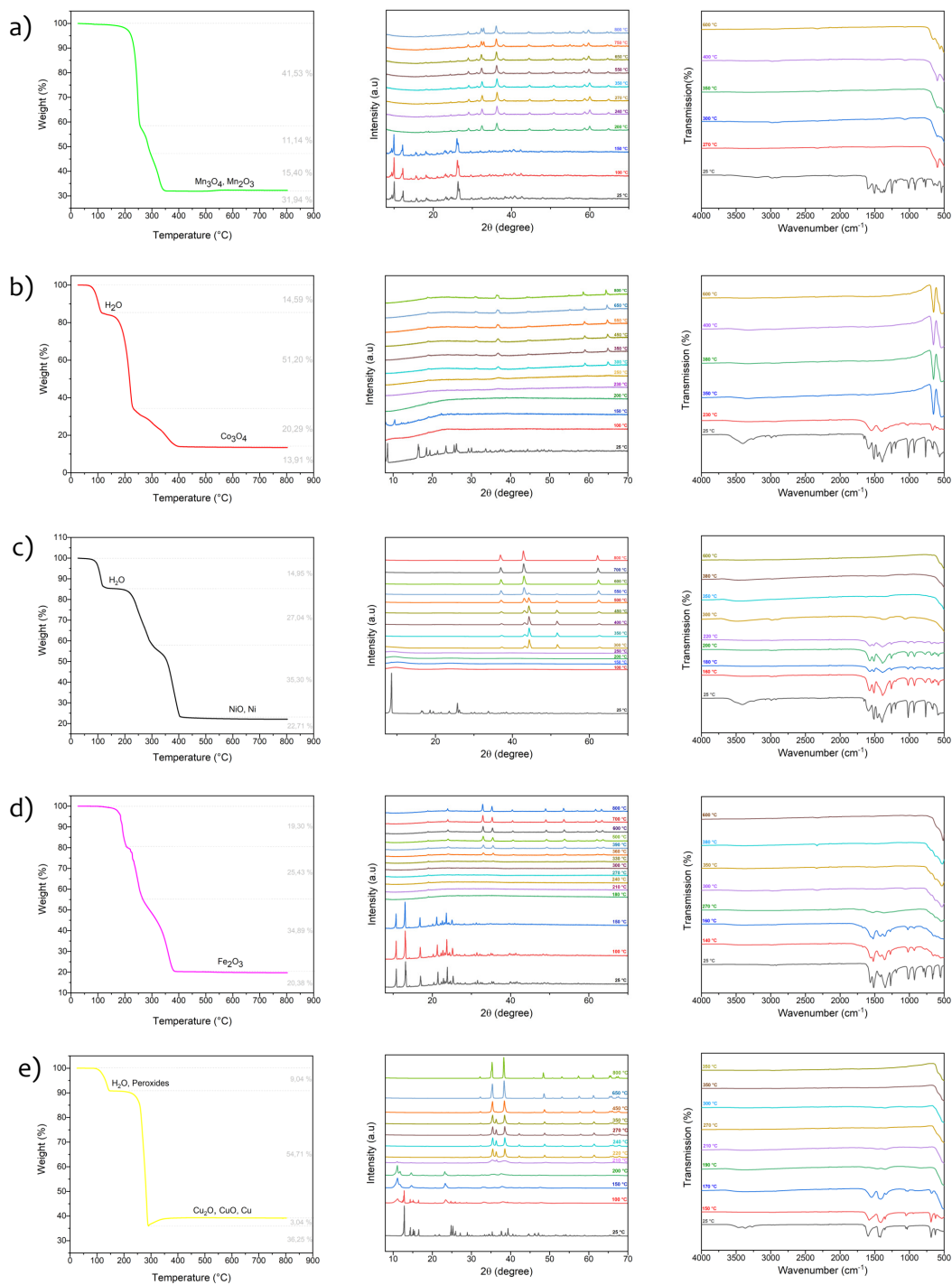


Figure 4.3: From left to right TGA, XRD and ATR-FTIR graphs of the precursors. a) Mn(acac)₂, b) Co(acac)₃, c) Ni(acac)₂, d) Fe(acac)₃ and e) Cu(ac)₂. The TGA and XRD were generated at air and a heating rate of 5 °C/min.

characteristic spectra of an oxide appears. The used precursor contained Mn^{2+} and the generated oxide contain a mixture of Mn^{2+} and Mn^{3+} . Thus, an partial oxidation of the manganese has taken place. As the thermal decomposition was taken place under air flow. Thus, an oxidative atmosphere.

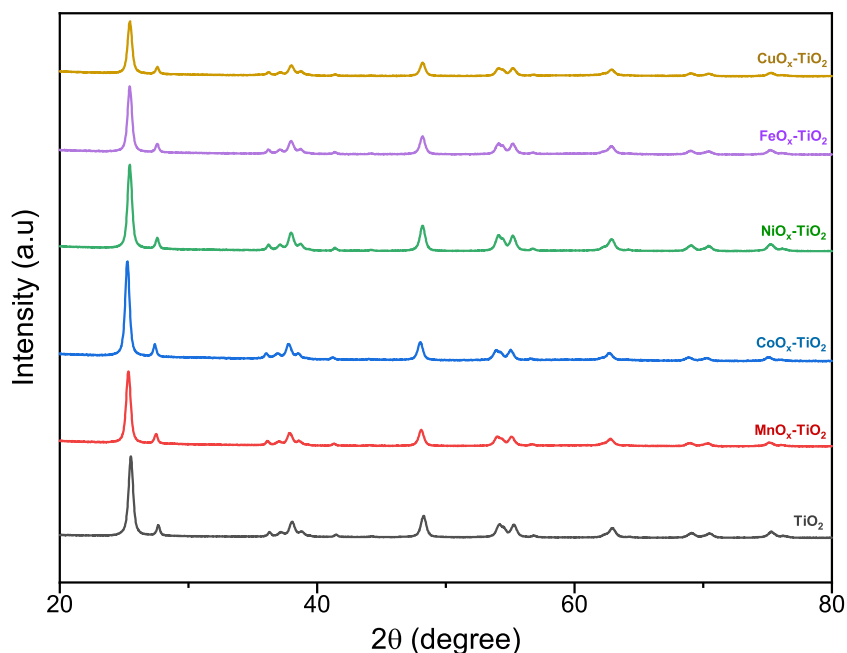


Figure 4.4: Diffractogram of the EtOH, Air synthesised $\text{MO}_x\text{-TiO}_2$ composites and heat treated at 350 °C for 10 h and TiO_2 as reference. In these diffractograms both phases of TiO_2 are visible, rutile and anatase.

Figure 4.3b shows the $\text{Co}(\text{acac})_3$ analysis. The TGA revealed first the loss of the two water molecules coordinated to the salt, which is visible in the FTIR spectra by the characteristic broad band at 3404.69 cm^{-1} . These at 116 °C are completely evaporated and the decomposition of the acetylacetonates begins ending at 402 °C with the Co_3O_4 generation, confirmed by XRD and FTIR. Here again, a mixed oxidation state oxide (Co_3O_4) was generated containing Co^{2+} and Co^{3+} . Hence, a partial reduction of the cobalt has taken place, as the precursor was Co^{3+} . The reason for this reduction is probably that the acetylacetonates decomposes through a radical formation, inducing so the reduction of the metal. This decomposition mechanism was reported in previous studies for $\text{Cu}(\text{ac})_2$ where the same was observed.⁶⁵

Similar behaviour is observable for the other salts (figure 4.3c, d and e). Where

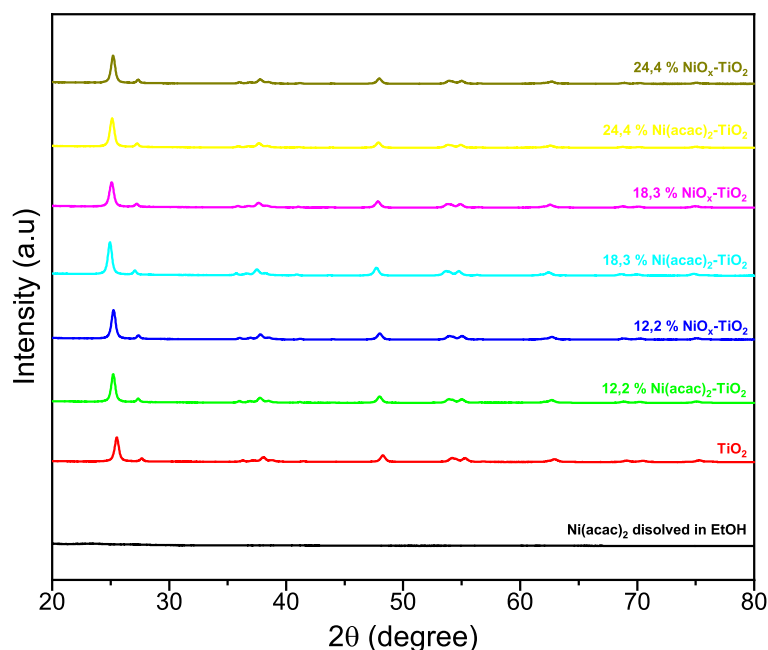


Figure 4.5: XRD diffractogram of the Ni enriched composites and $\text{Ni}(\text{acac})_2$ after dissolved in EtOH at air. Both diffractograms are shown of the composites samples: without thermal treatment and after 350 °C for 10 h thermal decomposition.

$\text{Ni}(\text{acac})_2$ loses the two coordinated water molecules until 119,5 °C. Then, from 119,5 °C the acetylacetonates decomposes until 406 °C leading to the formation of NiO and metallic Ni. The XRD data show that Ni is present until 550 °C, then all metallic Ni get oxidized to NiO. Again, a reduction has taken place, where the responsible is probably the radical intermediate of the acetylacetonate decomposition. Then by further increasing the temperature under air flow it gets oxidized again the metallic Ni to NiO. $\text{Fe}(\text{acac})_3$ is stable until 143 °C then the decomposition of the acetylacetonate starts until 387 °C, when Fe_2O_3 is formed. This is confirmed by complementary XRD and FTIR experiments. Once more, a mixed oxide was obtained by the acetylacetonate intermediate decomposition products. The last one, $\text{Cu}(\text{ac})_2$ begins the dehydration already at 91 °C ending at 146 °C. The decomposition of the acetate is from 216,5 °C until 291 °C with the formation of CuO, Cu_2O and metallic Cu. Then a sharp increase of the mass takes place which is generated due to the partially oxidation of Cu_2O and Cu to CuO. Again, as mentioned before, the generation of the metallic Cu and Cu_2O ,

is related to the decomposition through radical formation of the acetate. And the later re-oxidation induced by the temperature increase under air flow.

The XRD analyses of the $\text{MO}_x\text{-TiO}_2$ composites suggest that the oxides on the TiO_2 have an amorphous structure as the signals correspond only to the two phases of TiO_2 : rutile and anatase (figure 4.4). In order to avoid misinterpretation due to low concentration, undetectable with standard XRD, model samples enriched with Ni (12.2 %, 18.3 % and 24.4 % in Ni) were prepared and investigated. In addition to avoid misinterpretation due to overlapping of the signals both samples before and after heat treatment were measured. These revealed (figure 4.5) that all samples showed no differences from TiO_2 again. This could be explained by loss of crystallinity which can have several reasons. One, is that the precursor salt loses crystallinity due to dissolution. This makes sense as the solvent is evaporated under stirring. Thus, no crystals can be formed and an amorphous structure is generated. This was confirmed by XRD analysis (figure 4.5) that the dissolved salts indeed loses crystallinity under this synthesis conditions. The other possibility is that the salt is adsorbed on the surface of the TiO_2 substrate in a not ordered way causing this amorphicity. Hence, it can be suggested that the absence of a signal different than for rutile and anatase is due to non crystallinity of the adsorbed metal oxides on the crystalline TiO_2 . Thus, it was not possible to determine the salt decomposition products on the composites by XRD. For these reason, the behaviour of the salt precursors were taken as guideline for the oxides that could be generated on the TiO_2 nanoparticles.

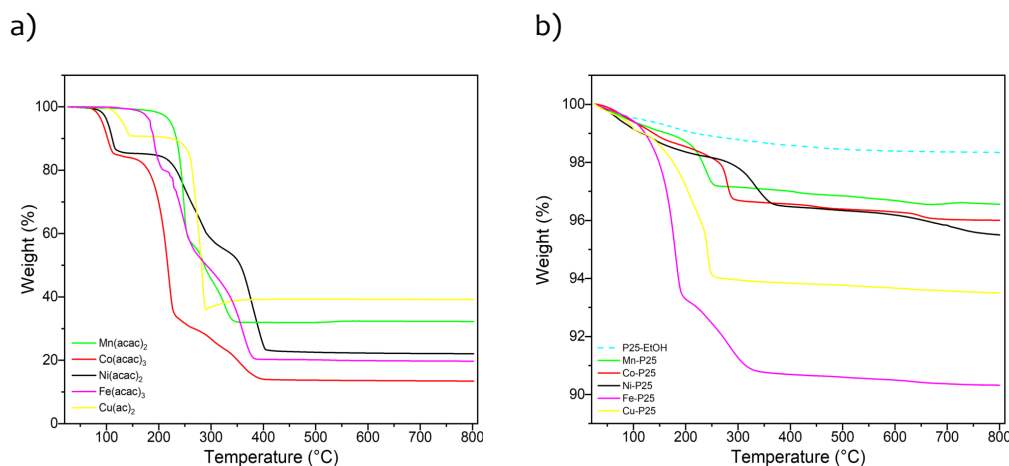


Figure 4.6: TGA a) of the precursors and b) of the composites. Measured at air and a heating rate of 5 °C/min.

Anatase has shown to be the more photocatalytic active phase of TiO_2 .⁶⁶ As the exciton diffusion length is twice longer than for rutile.⁶⁷ Thus, leading to

lower recombination of the electron-hole pair and so increased activity. At normal pressure condition and temperatures below 400 °C, anatase is the main constituent. At higher temperatures the transition into rutile phase takes place.⁶⁸ Thus, in our study the goal was to generate the metal oxides attached on TiO₂ avoiding these transition at 400 °C. The ATR FT-IR analyses for the pure salt precursors (figure 4.3) show that at 350 °C all organic part was striped away and the XRD confirmed the formation of the corresponding oxides. To determine the thermal treatment effect also lower temperatures were taken where the conversion took place. These lower temperatures were 300 °C for Ni(acac)₂, 230 °C for Co(acac)₃ and 270 °C for Mn(acac)₂, Fe(acac)₃ and Cu(ac)₂. The TGA of the synthesised composites (figure 4.6) revealed that the main decomposition took place at these temperatures.

4.2 Characterisation of the MO_x–TiO₂ composites

4.2.1 TEM analyses

The verification of attached metal oxides nanoparticles on TiO₂ was accomplished with TEM. As the SEM resolution was not enough to reveal the presence of the attached MO_x nanoparticles, with intended size up to few nm. So TEM confirmed the generation of small surface nanoparticles for all samples. However, the distribution of the MO_x nanoparticles was not homogeneous. In figure 4.7 the MnO_x–TiO₂, EtOH-air sample is shown. Figure 4.7a represents the pure TiO₂ and b) - c) are part of the same sample. There it is observable a huge amount of MnO_x nanoparticles in c), while in b) they are totally absent. A possible explanation for this behaviour is that the interaction of MnO_x–TiO₂ is from a weaker nature than MnO_x–MnO_x when synthesised in EtOH at air. Thus, leading to separate particles and so the accumulation in one region of the sample. In figure 4.8 it is shown all Mn containing samples. There a) corresponds to TiO₂ as reference while b) and e) to the H₂O–Air and EtOH–N₂ samples, respectively. These samples revealed that no MnO_x nanoparticles at all were formed. In c) and f), which corresponds to the H₂O–N₂ and EtOH-Vacuum samples, respectively, small MnO_x nanoparticles were observable as highlighted in the image.

As comparison to the MnO_x–TiO₂ also all the CoO_x–TiO₂ synthesised samples were characterized by TEM (Figure 4.9). Here image a) is the TiO₂ as reference again. b) corresponds to the H₂O–air sample, which was the only one where no CoO_x nanoparticles were observable. All the other samples showed the formation of small CoO_x nanoparticles. The image observable in f) corresponds to the EtOH-vacuum sample. This showed a distinct behaviour to the other samples by instead of forming random small CoO_x nanoparticles on the TiO₂, it coated the TiO₂. Suggesting, that the interaction for the EtOH, vacuum sample is of

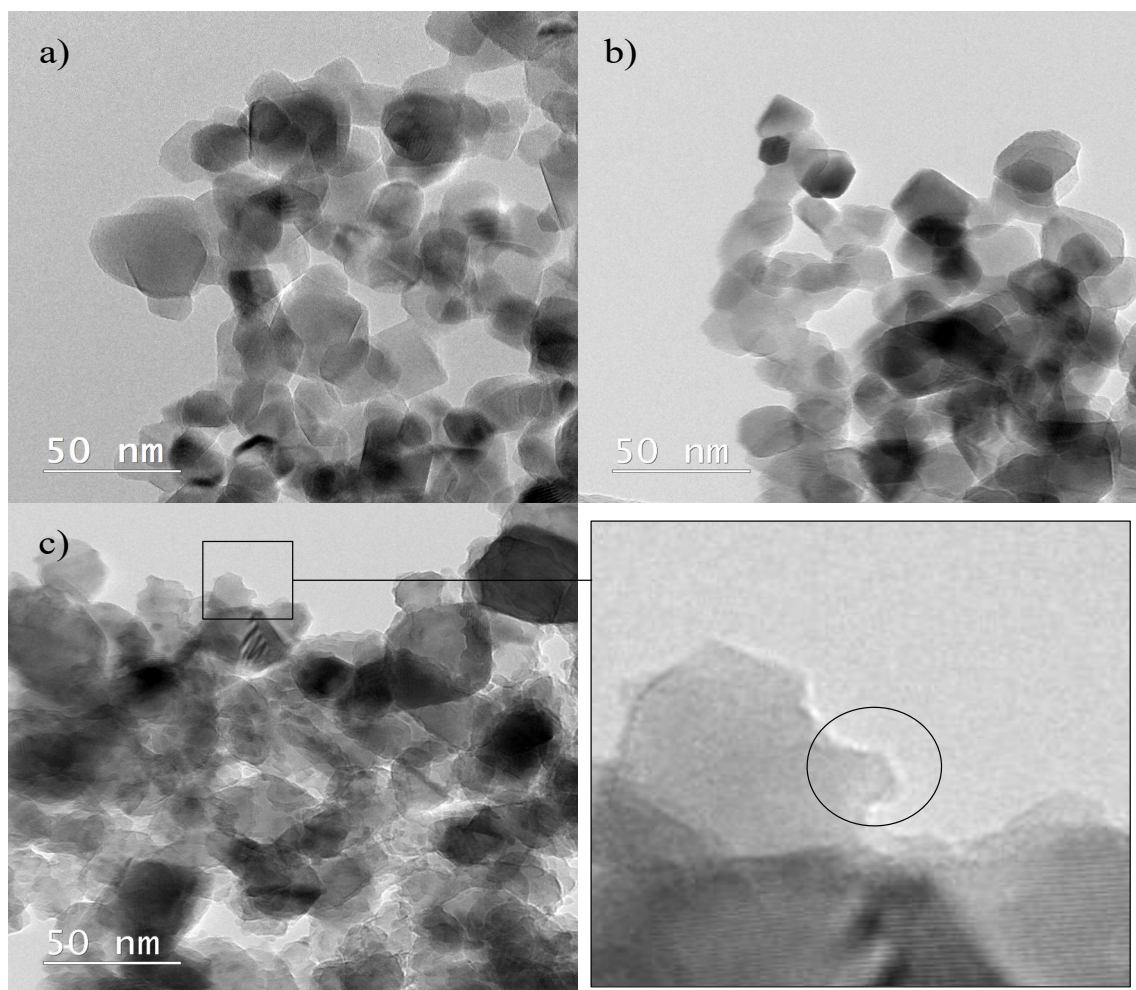


Figure 4.7: TEM images showing the MnO_x nanoparticles inhomogeneity of $\text{Mn}(\text{acac})_2 - \text{TiO}_2$ synthesised in EtOH, air at 350°C for 10 h. a) Is the pure TiO_2 , b) shows one part of the sample without any MnO_x nanoparticles and c) with a lot of MnO_x nanoparticles.

stronger nature between CoO_x and TiO_2 . While the other samples, where separated small CoO_x nanoparticles are formed, apparently attached to TiO_2 from one side, the interaction is weaker between TiO_2 and CoO_x nanoparticles. While the $\text{CoO}_x - \text{CoO}_x$ interaction is stronger. Leading to agglomerate on the TiO_2 surface, instead of a homogeneous coating of the TiO_2 nanoparticle. Thus, the different solvents and atmosphere affect the kind of interaction between the nanoparticles.

The TEM images revealed that the optimized synthetic protocol indeed generated MO_x nanoparticles on the TiO_2 . To determine the morphology and if MO_x nanoparticles were formed on TiO_2 in the other samples as well also TEM images were taken, but only from the EtOH-air samples (figure 4.11). Theses revealed

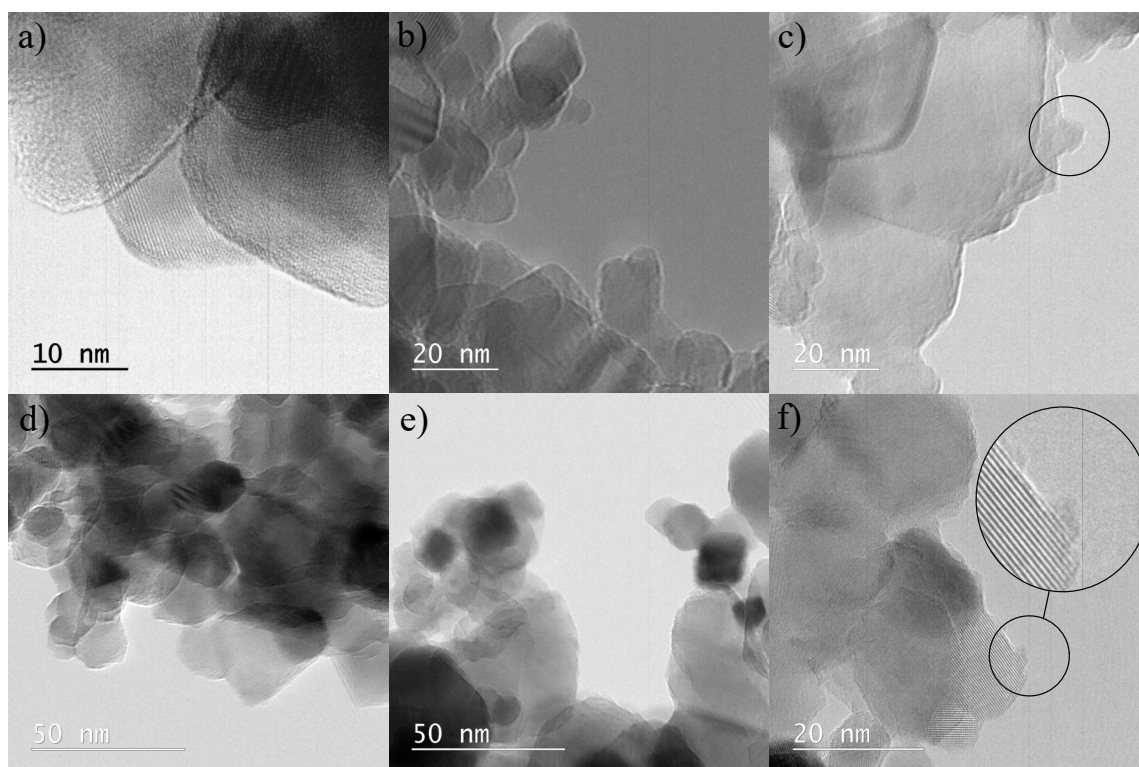


Figure 4.8: Comparison of the different $\text{MnO}_x - \text{TiO}_2$ samples for MnO_x nanoparticles generation. a) correspond to the pure TiO_2 , b) to the H_2O -air sample, c) H_2O - N_2 d) EtOH -air, e) EtOH - N_2 and f) EtOH -vacuum samples. c) and f) show the formation of clusters on the TiO_2 .

that the morphologies of the deposited $\text{CuO}_x - \text{TiO}_2$ and $\text{NiO}_x - \text{TiO}_2$ nanostructures behave the same way as the $\text{CoO}_x - \text{TiO}_2$ EtOH -vacuum sample (figure 4.9), covering the whole TiO_2 . While the $\text{FeO}_x - \text{TiO}_2$ sample showed also inhomogeneity, but with a higher concentration of MO_x nanoparticles than the $\text{MnO}_x - \text{TiO}_2$ sample.

The TEM data revealed that the different synthetic routes by changing the solvent and the presence of air, N_2 or vacuum affect the morphology and formation of those MO_x nanoparticles. Further, it revealed that another affecting parameter is which kind of salt and metal was used as all of them showed different behaviour. Hence, different strength of interaction between the nanoparticles is generated by the different method, salts and metals.

The detailed study of the obtained data from TEM revealed that the generated MO_x nanoparticles had an amorphous nature, as already mentioned in section 4.1.1. But on the $\text{CoO}_x - \text{TiO}_2$ H_2O - N_2 few CoO_x nanoparticles were seen that showed certain crystallinity (figure 4.10). By deeper examination of those CoO_x

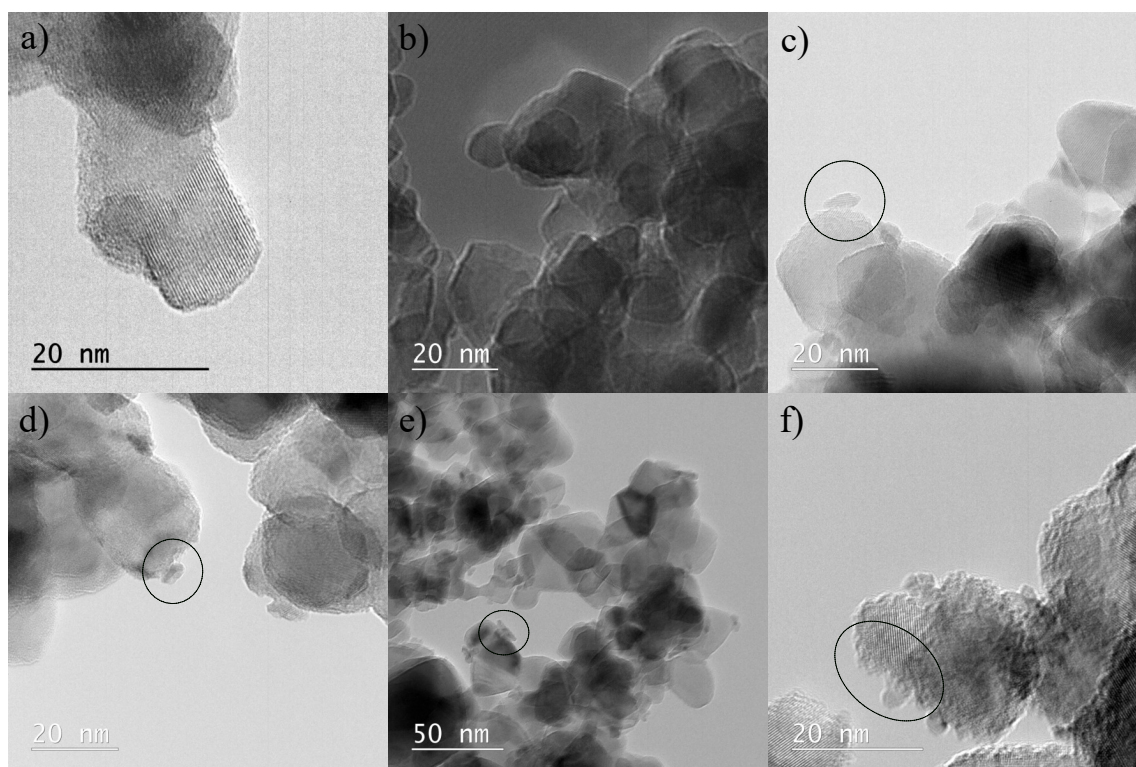


Figure 4.9: Comparison of the different $\text{CoO}_x - \text{TiO}_2$ samples for CoO_x nanoparticles generation. a) correspond to the pure TiO_2 , b) to the H_2O -air sample, c) $\text{H}_2\text{O}-\text{N}_2$ d) EtOH -air, e) $\text{EtOH}-\text{N}_2$ and f) EtOH -vacuum samples. c) - f) show the formation of clusters on the TiO_2 .

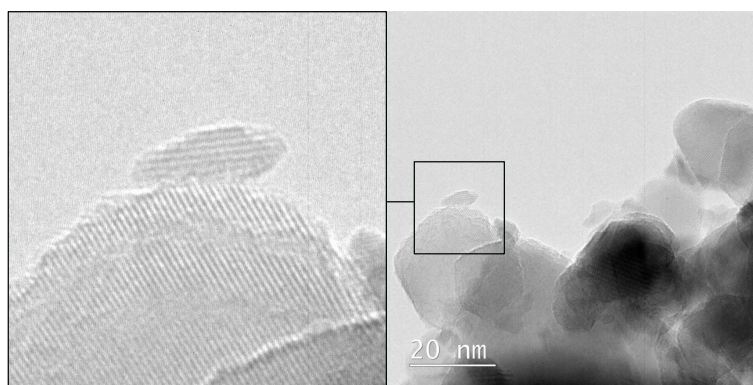


Figure 4.10: $\text{CoO}_x - \text{TiO}_2$, $\text{H}_2\text{O}-\text{N}_2$ sample where it is visible that one of the CoO_x nanoparticles shows crystallinity.

nanoparticles it was determined an inter-planar spacing value of 4.7 \AA . This value was compared with the acta crystallographica B58 database and showed to corre-

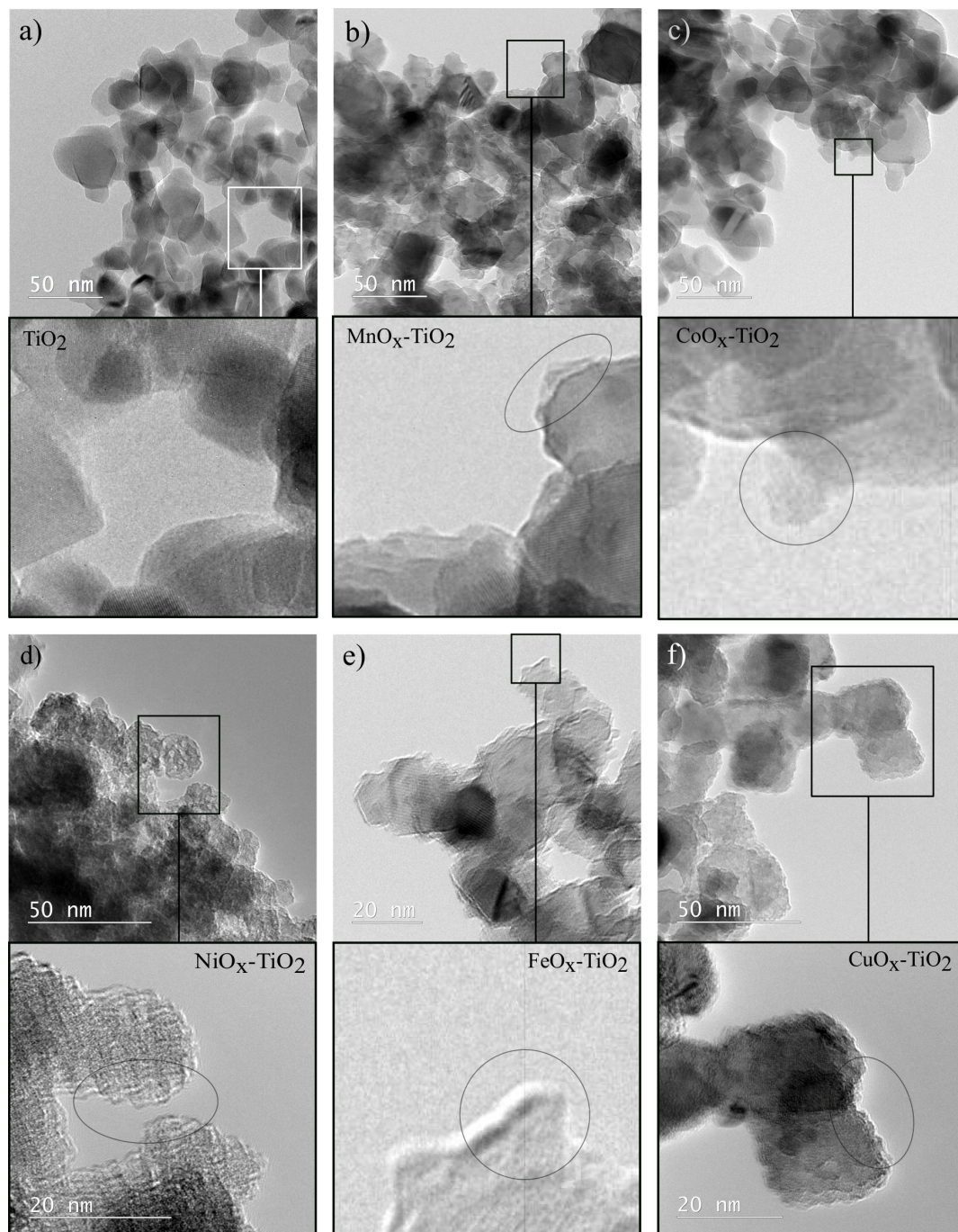


Figure 4.11: Comparison of the different MO_x - TiO_2 samples for MO_x nanoparticles generation and shape. All samples were synthesised in EtOH, air, 350 °C for 10 h. a) correspond to the pure TiO_2 , b) to the MnO_x - TiO_2 , c) CoO_x - TiO_2 , d) NiO_x - TiO_2 , e) FeO_x - TiO_2 and f) CuO_x - TiO_2 .

spond to the Co_3O_4 . With this it can be concluded that at least the crystalline CoO_x nanoparticles correspond to this oxide. The formation of these few crystalline CoO_x nanoparticles and the rest amorphous can be explained by that the salt co-precipitated with TiO_2 or being adhered on TiO_2 , respectively. The synthesis was carried out by evaporation of the solvent while the solution was stirring. Thus, no possibility for the salt to form a crystals. By making the heat treatment for 10 h these can begin to reorganize and form a crystal. However, if the acetylacetonates/acetate and the metals are strongly attached to the TiO_2 substrate these will not easily reorganize to form a crystal. Thus, also after heat treatment for 10 h no crystallinity is observable by the MO_x nanoparticles on TiO_2 . Hence, it can be suggested that these Co_3O_4 are not adhered on the TiO_2 substrate, while the amorphous part is.

4.2.2 TG analysis

4.2.2.1 TGA comparison of the pure metal salts and the salt attached on TiO_2 composites

To extract further information about the composite thermal behaviour TGA of all metal salts attached on TiO_2 was performed. In figure 4.12 TGA of the pure precursor salt and attached on TiO_2 are plotted for comparison.

The TGA of $\text{Mn}(\text{acac})_2$ revealed that the precursor salt is thermally stable until 223 °C, leading to the decomposition of the salt until 347 °C where the oxides are generated. For the $\text{Mn}(\text{acac})_2\text{-TiO}_2$ composite a different behaviour is observed: decomposing from the very beginning, 25 °C, and continues until 258 °C. Then the sample mass continues to slowly decrease until 800 °C without stabilizing. This behaviour was not observed for the pure precursor and is likely related to a different state of the precursor on the composite sample.

The $\text{Co}(\text{acac})_3$ salts shows thermal stability until 65.5 °C when the decomposition of the crystalline water starts reaching the end at 109 °C. After this step the decomposition of the acetylacetonates begins, ending at 393 °C with the oxide formation. Again the composite behaves different by starting the decomposition at 25 °C with a drop in mass until 290 °C. Finally the decomposition continues with a small constant decrease in mass loss until 685 °C when a mass equilibrium is reached.

$\text{Ni}(\text{acac})_2$ behaves similar than $\text{Co}(\text{acac})_2$, not decomposing until 76.7 °C when evaporation of the crystalline water starts and proceeds until 140 °C. The acetylacetonates decomposition happens between 176 °C and 405 °C yielding to the corresponding oxides. Once again, the composite behaves in another way. The $\text{Ni}(\text{acac})_2\text{-TiO}_2$ decomposition initiates already from the very beginning with a huge decrease in mass from 241 °C until 365 °C, continued by a slow decomposition

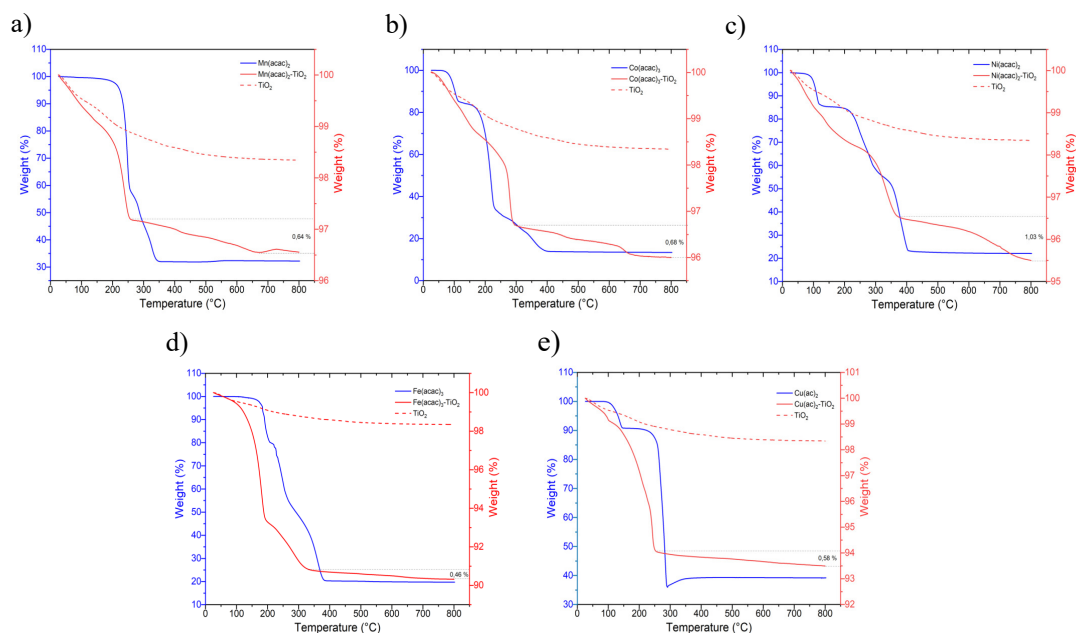


Figure 4.12: Comparison of the TGA of the metal salt and attached on TiO_2 . TGA data generated with a heating rate $5\text{ }^\circ\text{C}/\text{min}$ and at air. The right y axes correspond to the pure salt, while the left y axes correspond to the composite. a) $\text{Mn}(\text{acac})_2$ and $\text{Mn}(\text{acac})_2\text{-TiO}_2$, b) $\text{Co}(\text{acac})_3$ and $\text{Co}(\text{acac})_3\text{-TiO}_2$, c) $\text{Ni}(\text{acac})_2$ and $\text{Ni}(\text{acac})_2\text{-TiO}_2$, d) $\text{Fe}(\text{acac})_3$ and $\text{Fe}(\text{acac})_3\text{-TiO}_2$ and e) $\text{Cu}(\text{ac})_2$ and $\text{Cu}(\text{ac})_2\text{-TiO}_2$.

until $800\text{ }^\circ\text{C}$ with no mass stabilization.

For $\text{Fe}(\text{acac})_3$ the acetylacetonates decomposes between $112\text{ }^\circ\text{C}$ and $290\text{ }^\circ\text{C}$ leading to the corresponding oxide without further mass loss of the salt. $\text{Fe}(\text{acac})_3\text{-TiO}_2$ on the other side, showed to have a lower decomposition in the beginning, compared to the previous discussed composites. After this, it shows a steep slope until $345\text{ }^\circ\text{C}$, ending with a certain stabilization until $800\text{ }^\circ\text{C}$ with a very slow decrease in mass.

The last precursor, $\text{Cu}(\text{ac})_2$, started losing the water between $87\text{ }^\circ\text{C}$ and $154\text{ }^\circ\text{C}$. This is followed by the decomposition of the acetate starting at $198\text{ }^\circ\text{C}$ and ending at $290\text{ }^\circ\text{C}$ with the oxide generation. From here a mass increase is observable until $360\text{ }^\circ\text{C}$ due to the oxidation of Cu and Cu_2O to CuO . The composite behave different, decomposing from the beginning until $251\text{ }^\circ\text{C}$, followed by a slow decrease in mass reaching only a certain stabilization at the end.

These graphs revealed that indeed the composites behave different with respect to the pure precursor. One important difference is that $\text{Co}(\text{acac})_3$, $\text{Ni}(\text{acac})_2$ and $\text{Cu}(\text{ac})_2$ are losing the crystalline water at the beginning, while for $\text{CoO}_x\text{-TiO}_2$, $\text{NiO}_x\text{-TiO}_2$ and $\text{CuO}_x\text{-TiO}_2$ this is not the case. Thus, it can be speculated that

the crystalline water was not adsorbed on the TiO_2 surface after solubilized the salts, being removed by the solvent, EtOH. Another important difference is that all composites start the decomposition from the very beginning, 25 °C, while for the pure salts this is not the case: they are stable until a certain range of temperature before the decomposition starts. The pure TiO_2 show similar behaviour at the beginning, losing mass already from the start, 25 °C. Thus, this behaviour by losing mass from the very beginning could be related to TiO_2 by the adsorption of dust, solvent, etc. In addition, the precursors showed a mass stabilization, with no further mass loss, at the end of the decomposition, which is not the case for the composites. As such $\text{MnO}_x-\text{TiO}_2$ at the last step of the decomposition is still losing 0,64 % of mass. Although, a certain stabilization was reached at the very end. The same was observed for $\text{CoO}_x-\text{TiO}_2$ despite the 0,68 % mass loss. $\text{FeO}_x-\text{TiO}_2$ and $\text{CuO}_x-\text{TiO}_2$ showed a very slow decrease of the mass, 0,46 % and 0,58 % respectively until 800°C. Thus, slow decomposition of the composite still continues. The one with the highest slope at the end of the decomposition is $\text{NiO}_x-\text{TiO}_2$ with 1,03 % of mass loss still without even apprehend to reach a certain stabilization. These behaviour of the composites at higher temperatures is possibility related to the decomposition products of the acetylacetonates, which will be further discussed in the next section 4.2.2.2. In conclusion, this data revealed that the composites are decomposing from the beginning, 25 °C, until almost the end, 800°C, which confirms that the decomposition mechanism is different of the pure salt and when adsorbed on the TiO_2 substrate.

4.2.2.2 TG analysis of the metal salt – TiO_2 composites

To further extract information from the TGA of the metal salt – TiO_2 composites we performed theoretical estimations of the final residual mass and the intermediate mass losses that would correspond to potential generated oxides and other decomposition products. These calculations were done as described elsewhere⁶⁹ and using the TGA of the pure precursors as reference. The total mass loss of the composite decomposition was extracted experimentally from the composite TGA curves. The residual mass was possible to extract by knowing the used concentration of precursor for the synthesis and the mass loss from the TGA.

$\text{Mn}(\text{acac})_2-\text{TiO}_2$

Figure 4.13 shows the TGA of the $\text{Mn}(\text{acac})_2-\text{TiO}_2$ composite and table 4.1 the corresponding theoretical calculated mass loss and residual mass. The TGA shows the different behaviour of the composite with respect to the pure TiO_2 . The decrease in mass % of the pure TiO_2 corresponds to adsorbed species on the surface,^{11,12,61} as the only possible conversion of TiO_2 at these condition is from anatase to

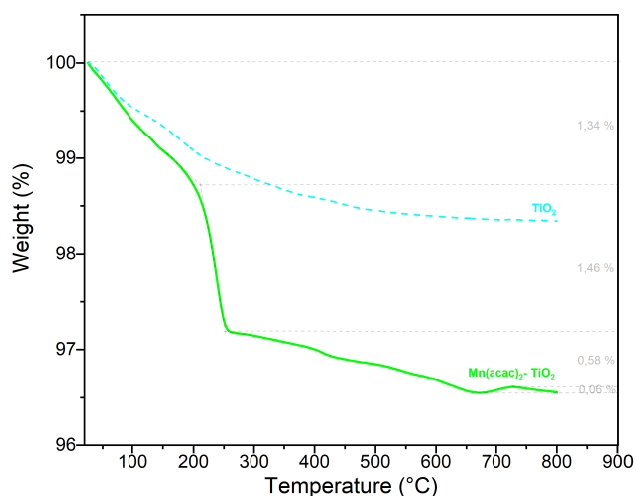


Figure 4.13: TGA of the $\text{Mn}(\text{acac})_2$ - TiO_2 composite synthesised in EtOH/air and TiO_2 as reference previously dissolved in EtOH/air like the composite. Heating rate $5\text{ }^\circ\text{C}/\text{min}$ in air. The total mass loss corresponds to 3.44 %. The initial amount of $\text{Mn}(\text{acac})_2$ in the composite is 13.6 % in mass leading to a residual mass of 10.16 %.

Table 4.1: Theoretical calculation for the possible manganese compounds and decomposition products generated of the $\text{Mn}(\text{acac})_2$ - TiO_2 composite. The experimental obtained total mass loss % is 3.44 % and the residual mass % is 10.16 %.

	Mass loss (%)	Residual mass (%)
Mn	-	2.95
MnO	-	3.81
MnO ₂	-	4.67
Mn ₂ O ₃	-	4.24
Mn ₃ O ₄	-	4.09
Acetylacetonate	5.38 *	-
	10.76 **	-
Oxygen	0.86 *	-
	1.72 **	-

* One time this molecule.

** Two times this molecule.

rutile,⁶⁸ meaning no mass loss is expected. Thus, the observed slope at the beginning of the composite i.e. from $25\text{ }^\circ\text{C}$ to $199\text{ }^\circ\text{C}$ could correspond also to adsorbed species. The slope from $199\text{ }^\circ\text{C}$ to $259\text{ }^\circ\text{C}$ could then correspond to the decompo-

sition of the acetylacetonate, as previous mentioned in section 4.1.1 for the pure precursor. However, the calculated values for one and two acetylacetonates (table 4.1) do not correspond to the total mass loss of 3.44 % experimentally observed. Further, the theoretical calculated residual mass of the possible compounds generated are much below the actually experimentally obtained residual mass of 10.16 %. A possible explanation for these difference in the calculated values and the experimentally obtained is that the decomposition of the acetylacetonates takes place on the TiO_2 and the products remain adsorbed on it, which then further decomposes in other species. This would also explain the continued decreases of the the mass % at higher temperatures.

$\text{Co}(\text{acac})_3-\text{TiO}_2$

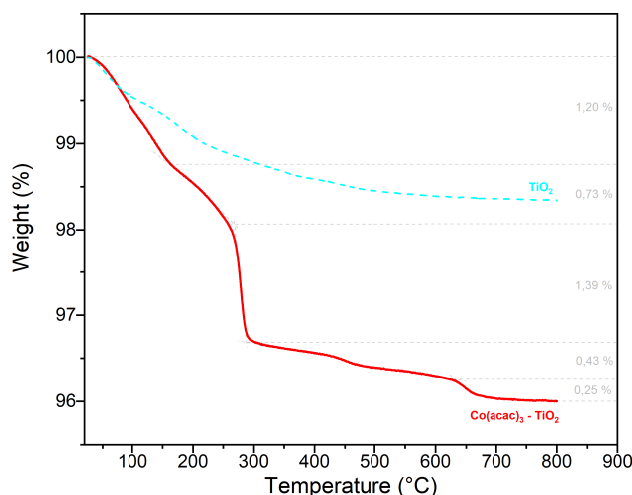


Figure 4.14: TGA of the $\text{Co}(\text{acac})_3-\text{TiO}_2$ composite synthesised in EtOH/air and TiO_2 as reference previously dissolved in EtOH/air like the composite. Heating rate 5 °C/min in air. The total mass loss corresponds to 4.0 %. The initial amount of $\text{Co}(\text{acac})_3$ in the composite is 15.9 % in mass leading to a residual mass of 11.9 %.

$\text{Co}(\text{acac})_3-\text{TiO}_2$ shows a similar behaviour than $\text{Mn}(\text{acac})_2-\text{TiO}_2$ (figure 4.14) with a starting slope from 25 °C to 259 °C which could correspond again to adsorbed species on the nanoparticles surface or a slow decomposition of the salt. Then the sharp slope from 259 °C to 310 °C could correspond to the partial decomposition of acetylacetonate as it did the pure precursor in section 4.1.1. Again, the calculated values and the experimentally obtained do not fit (table

Table 4.2: Theoretical calculation for the possible cobalt compounds and decomposition products generated of the $\text{Co}(\text{acac})_3\text{-TiO}_2$ composite. The total mass loss corresponds to 4.0 %. The initial amount of $\text{Co}(\text{acac})_3$ in the composite is 15.9 % in mass leading to a residual mass of 11.90 %.

	Mass loss (%)	Residual mass (%)
Co	-	2.61
CoO	-	3.32
Co ₂ O ₃	-	3.67
Co ₃ O ₄	-	3.55
Acetylacetonate	4.42 *	-
	8.86 **	
	13.26 ***	-
Oxygen	0.71 *	-
	1.42 **	
	2.13 ***	-

* One time this molecule.

** Two times this molecule.

*** Three times this molecule.

4.2). The total mass loss corresponds to 4.0 % while the expected mass loss for the three acetylacetonates is about 13.26 %. The residual mass is also much below the experimental value of 11.9 %. This suggest that the main part of the decomposition products of the acetylacetonate remains adsorbed on the composite. Although, in section 4.2.1 the TEM image (figure 4.10) showed that Co_3O_4 nanoparticles were observed on the TiO_2 . This confirms that oxides are indeed generated. A possible reason for this contradiction is that the generated Co_3O_4 oxide comes from not adsorbed salt on the TiO_2 after the synthesis of the nanoparticles. With other words, by synthesising the nanoparticle-cluster composites the acetylacetonates anions and the metal cations were adsorbed on the TiO_2 substrate. Then after the heat treatment these decomposes on it in the corresponding products. However, some of the acetylacetonates and metal ions is possible that they precipitated separately without being attached on the TiO_2 . Thus, by thermally treat them, they will behave as the pure salt, generating the oxide. While the one attached will generate the amorphous clusters with probably different morphology. Therefore, these observed Co_3O_4 oxide is possibly not attached to the TiO_2 .

Ni(acac)₂-TiO₂

The $\text{Ni}(\text{acac})_2\text{-TiO}_2$ TGA is presented in figure 4.15 and the corresponding calculated data in table 4.3. It is possible to notice again this slope from the beginning

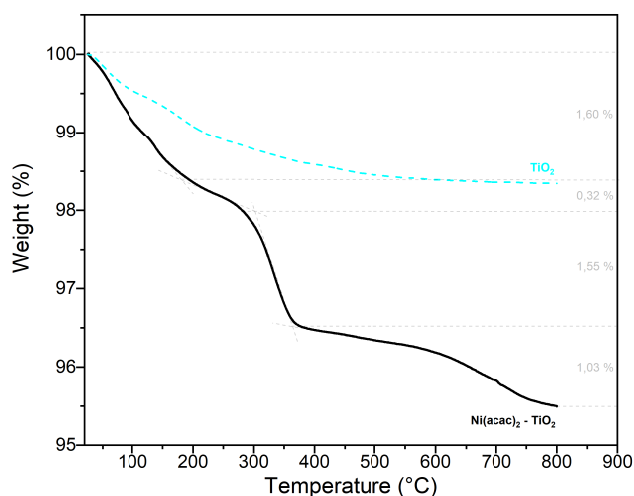


Figure 4.15: TGA of the $\text{Ni}(\text{acac})_2\text{-TiO}_2$ composite synthesised in EtOH/air and TiO_2 as reference previously dissolved in EtOH/air like the composite. Heating rate $5\text{ }^\circ\text{C}/\text{min}$ in air. The total mass loss corresponds to 4.5 %. The initial amount of $\text{Ni}(\text{acac})_2$ in the composite is 6.8 % in mass leading to a residual mass of 2.3 %.

Table 4.3: Theoretical calculation for the possible nickel compounds and decomposition products generated of the $\text{Ni}(\text{acac})_2\text{-TiO}_2$ composite. The total mass loss corresponds to 4.5 %. The initial amount of $\text{Ni}(\text{acac})_2$ in the composite is 6.8 % in mass leading to a residual mass of 2.3 %.

	Mass loss (%)	Residual mass (%)
Ni	-	1.55
NiO	-	1.98
NiO ₂	-	2.40
Ni ₂ O ₃	-	2.38
Acetylacetonate	2.65 *	-
	5.30 **	-
Oxygen	0.42 *	-
	0.84 **	-

* One time this molecule.

** Two times this molecule.

of the graph from $25\text{ }^\circ\text{C}$ to $283\text{ }^\circ\text{C}$ which again could be related to the dust, solvent, etc. adsorbed on the nanoparticles, or already the decomposition of the acetylacetonates. The second slope ranges than from $283\text{ }^\circ\text{C}$ to $370\text{ }^\circ\text{C}$. The ex-

perimental data has a total mass loss corresponding to 4.5 % and the calculated mass loss for two acetylacetonates is 5.3 %. The residual mass, from an 6.8 % of $\text{Ni}(\text{acac})_2$ initially on the TiO_2 , is about 2.3 %. The calculated residual mass of the NiO_2 , Ni_2O_3 and NiO are very close to this value. These numbers suggest, in difference to $\text{Mn}(\text{acac})_2 - \text{TiO}_2$ and $\text{Co}(\text{acac})_3 - \text{TiO}_2$, that most of the acetylacetonate and its decomposition products was removed from the TiO_2 surface, and that the generated remaining products could correspond to Ni oxides. The TEM pictures from section 4.2.1, picture 4.11, showed a difference in the morphology of the generated clusters on the TiO_2 . There, while $\text{Mn}(\text{acac})_2 - \text{TiO}_2$ and $\text{Co}(\text{acac})_3 - \text{TiO}_2$ showed the formation of nanoparticle clusters, $\text{Ni}(\text{acac})_2$ was totally covering the TiO_2 nanoparticles. Hereby, this indicates a possible correlation between the decomposition mechanism of the acetylacetonates salts and the morphology of the metal clusters on the TiO_2 . While for $\text{Mn}(\text{acac})_2 - \text{TiO}_2$ and $\text{Co}(\text{acac})_3 - \text{TiO}_2$ a lot of residual mass remains, for $\text{Ni}(\text{acac})_2 - \text{TiO}_2$ this is not the case. Leading to the conclusion that the later one, most of the organic part was removed after calcination. These would suggest that the presence of Ni is favouring the decomposition of the acetylacetonate on the TiO_2 and further desorption of the products. Also, that the Ni compounds are more strongly interacting with the TiO_2 surface than Mn and Co, as with the Ni species TiO_2 is coated, while for the Co and Mn species not.

$\text{Fe}(\text{acac})_3 - \text{TiO}_2$

Figure 4.16 and table 4.4 is shown the TGA and corresponding theoretical calculated data for $\text{Fe}(\text{acac})_3 - \text{TiO}_2$. This composite showed a different behaviour at the beginning with a less sharp slope at the start of just a mass loss of 0,82 %. Thus, it can be suggested that less dust, etc. was adsorbed at the surface. Then we have an inflection point at 197 °C and the next one at 322 °C which could correspond to the partial decomposition of the acetylacetonates as seen for the pure precursor in section 4.1.1. The experimental mass loss is 9.66 % while the calculated mass loss for three acetylacetonates is 15.9 %. The remaining residual mass after calcination is about 9.04 %. The calculated residual mass for the possible oxides is between 2.96 and 4.23 %. Thus, these data again do not match. These data suggest that a part of the decomposition products of the acetylacetonates remains on the nanopartilces. Although, the difference in the theoretical and experimental remaining mass is smaller for $\text{Fe}(\text{acac})_3 - \text{TiO}_2$ than for $\text{Mn}(\text{acac})_2 - \text{TiO}_2$ and $\text{Co}(\text{acac})_3 - \text{TiO}_2$. By looking at the TEM images in figure 4.11 again, it is possible to notice that these cluster present a morphology with a similarity in between the $\text{Mn}(\text{acac})_2 - \text{TiO}_2$ and $\text{Co}(\text{acac})_3 - \text{TiO}_2$, where separated nanoparticles are visible and $\text{Ni}(\text{acac})_2 - \text{TiO}_2$ and $\text{Cu}(\text{ac})_2 - \text{TiO}_2$ where a covered TiO_2 is visible. Thus, it can be speculated that the morphology of the clusters is related with the adsorp-

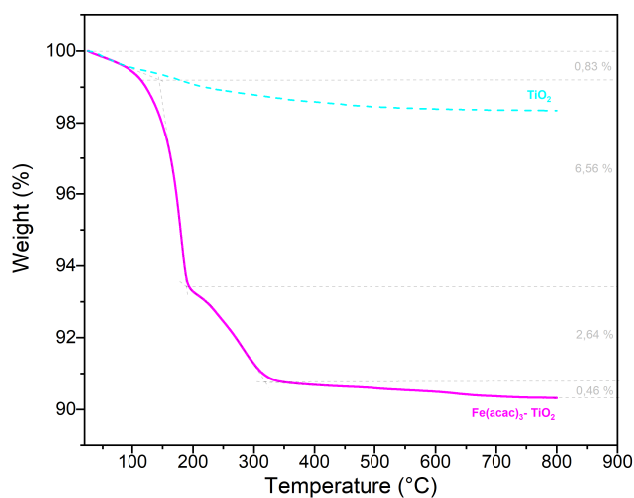


Figure 4.16: TGA of the $\text{Fe}(\text{acac})_3\text{-TiO}_2$ composite synthesised in EtOH/air and TiO_2 as reference previously dissolved in EtOH/air like the composite. Heating rate $5\text{ }^\circ\text{C}/\text{min}$ in air. The total mass loss corresponds to 9.66 %. The initial amount of $\text{Fe}(\text{acac})_3$ in the composite is 18.7 % in mass leading to a residual mass of 9.04 %.

Table 4.4: Theoretical calculation for the possible iron compounds and decomposition products generated of the $\text{Fe}(\text{acac})_3\text{-TiO}_2$ composite. The total mass loss corresponds to 9.66 %. The initial amount of $\text{Fe}(\text{acac})_3$ in the composite is 18.7 % in mass leading to a residual mass of 9.04 %.

	Mass loss (%)	Residual mass (%)
Fe	-	2.96
FeO	-	3.80
Fe_2O_3	-	4.23
Fe_3O_4	-	4.09
Acetylacetonate	5.30 *	-
	10.60 **	
	15.90 ***	
Oxygen	0.85 *	-
	1.70 **	
	2.55 ***	

* One time this molecule.

** Two times this molecule.

*** Three times this molecule.

tion/decomposition mechanism of the acetylacetonate on the nanoparticles and the metal. Suggesting here that the decomposition products of the acetylacetonate detach from the surface easier than the $\text{Mn}(\text{acac})_2\text{-TiO}_2$ and $\text{Co}(\text{acac})_3\text{-TiO}_2$, but much less than for $\text{Ni}(\text{acac})_2\text{-TiO}_2$, and the bonding of the Fe to the TiO_2 surface is from a weaker nature than Ni, but stronger than Mn and Co.

$\text{Cu}(\text{ac})_2\text{-TiO}_2$

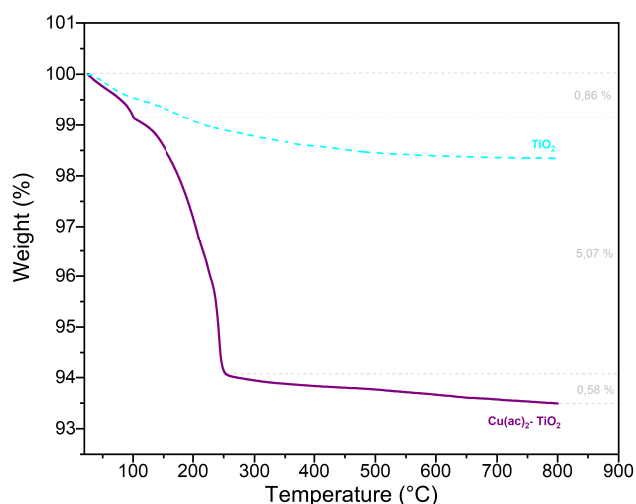


Figure 4.17: TGA of the $\text{Cu}(\text{ac})_2\text{-TiO}_2$ composite synthesised in EtOH/air and TiO_2 as reference previously dissolved in EtOH/air like the composite. Heating rate $5\text{ }^\circ\text{C}/\text{min}$ in air. The total mass loss corresponds to 6.51 %. The initial amount of $\text{Cu}(\text{ac})_2$ in the composite is 12.9 % in mass leading to a residual mass of 6.39 %.

The TGA of $\text{Cu}(\text{ac})_2\text{-TiO}_2$ is presented in figure 4.17 and the calculated data in table 4.5. The TGA shows a small slope at the beginning, ranging from $25\text{ }^\circ\text{C}$ to $102\text{ }^\circ\text{C}$ and the second slope from these point to $256\text{ }^\circ\text{C}$. The experimental total mass loss corresponds to 6.51 % while the corresponding one to the two acetates is about 8.39 %. The expected mass loss for two oxigens is about 2.27 %. Hence, by subtracting the two oxigens from the acetate the value corresponds then to 6.12 %, meaning, that the acetate was possibly decomposed remaining only the oxigens for the Cu oxide formation. Further, the calculated residual mass for the possible candidates, ranging from 4.51 to 5.65 %, are very similar to the experimental one of 6.39 %. Thus, equal than for the $\text{Ni}(\text{acac})_2\text{-TiO}_2$ composite, it can be speculated that the acetate was removed and the corresponding oxides

Table 4.5: Theoretical calculation for the possible copper compounds and decomposition products generated of the $\text{Cu}(\text{ac})_2\text{-TiO}_2$ composite. The total mass loss corresponds to 6.51 %. The initial amount of $\text{Cu}(\text{ac})_2$ in the composite is 12.9 % in mass leading to a residual mass of 6.39 %.

	Mass loss (%)	Residual mass (%)
Cu	-	4.51
CuO	-	5.65
Cu ₂ O	-	5.08
Acetylacetonate	4.19 *	-
	8.39 **	-
Oxygen	1.14 *	-
	2.27 **	-

* One time this molecule.

** Two times this molecule.

were generated on the TiO_2 substrate. The same similarities previously explained for the $\text{Ni}(\text{acac})_2\text{-TiO}_2$ composites by looking at the TEM picture in figure 4.11 are observable for the $\text{Cu}(\text{ac})_2\text{-TiO}_2$ composites and so similar conclusions.

4.2.3 XPS analyses

The previous XRD studies from section 4.1.1 of the composites revealed that the generated oxides on the substrate are amorphous. Thus, unfortunately it was not possible to extract information on the oxidation state, neither on the composition of the generated oxide clusters. For this reason XPS spectra were recorded for all composites.

In figure 4.18a the XPS survey spectrum of the $\text{MnO}_x\text{-TiO}_2$ is shown. The data contain a typical signal of the C 1s peak (figure 4.18b) which is always observable and corresponds to the adsorbed carbon species from the atmosphere. This C 1s spectrum was also separately recorded as reference to determine and adjust the correct parameters for the spectra. The measurements revealed that most of the samples exhibited strong charging effect during the data acquisition, so to compensate expected spectra shifts, a charge compensation gun was used. Nevertheless, a small Lorentzian broadening of the signal is visible with respect to the carbon fit, thus not complete characterization is possible from this spectra. In figure 4.18c and d the Mn spectra along with the Mn_2O_3 and MnO fit are shown, respectively. The data reveal that apparently both oxides fit with the observed spectra. The MnO fit seems to show the characteristic MnO satellite. Although, it is not possible to reliably determine which species is generated, it can be concluded that neither metallic Mn or MnO_2 was generated. Our conclusion can be supporter by other

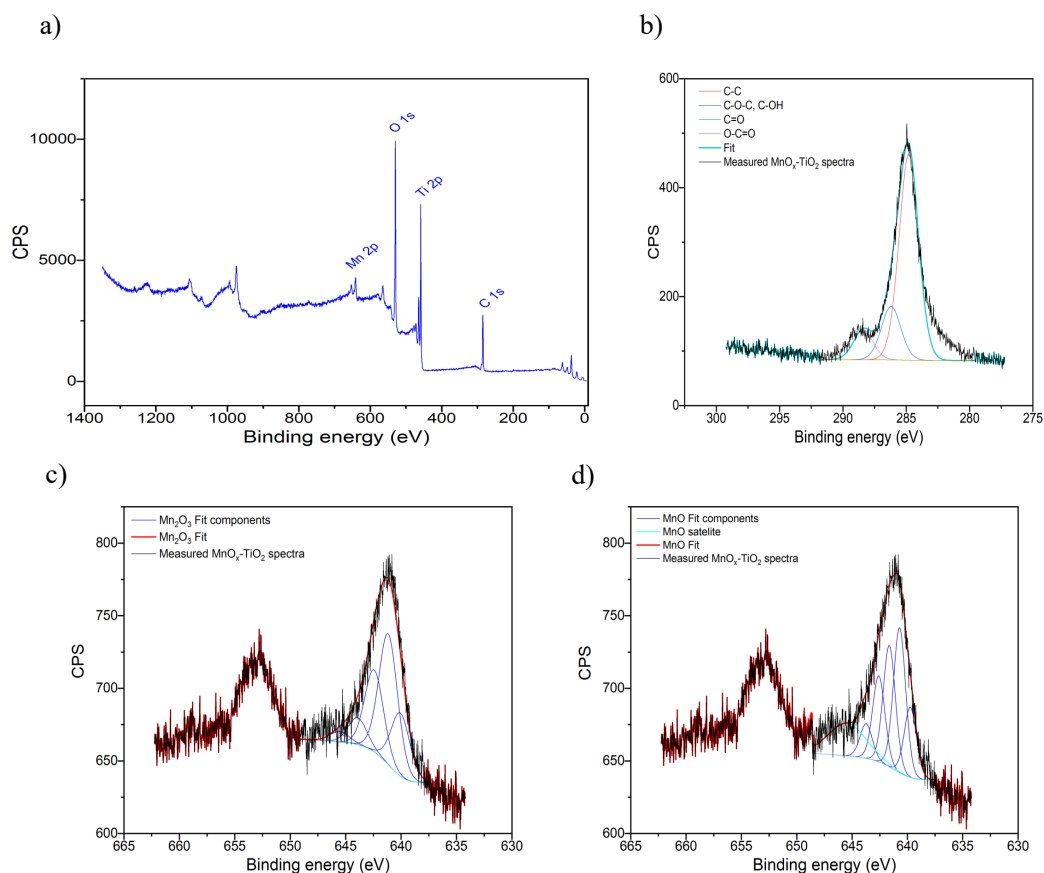


Figure 4.18: a) XPS survey spectrum of the $\text{MnO}_x\text{-TiO}_2$ treated at $350\text{ }^\circ\text{C}$ for 10 h. b) carbon spectra with the corresponding fit's. c) and d) Mn in the sample with the corresponding Mn_2O_3 and MnO fit's.

literature reports where similar compounds have been investigated.⁷⁰ Thus, it can be suggested that the composites contain a Mn(II) oxide species. The XRD of the pure precursor in figure 4.3 revealed that Mn_3O_4 is generated at $350\text{ }^\circ\text{C}$. Hence, it can be confirmed that the decomposition mechanism and the type of resulting species is different on the TiO_2 substrate with respect to the pure precursors.

The XPS survey spectrum of $\text{CoO}_x\text{-TiO}_2$ is shown in figure 4.19a and b) the characteristic C 1s peak again. The spectrum contains a low signal for Co which again impede a full characterisation despite the good fitting of the signal with the expected C 1s profile. c) and d) show the Co 2p signals of the composite. These by comparing the spectra with elsewhere⁷⁰ show the best fit with CoO and $\text{Co}(\text{OH})_2$ by having the characteristic satellite at 786 eV. While the metallic Co and Co_3O_4 spectra do not fit. Thus, it can be speculated that Co(II) is the

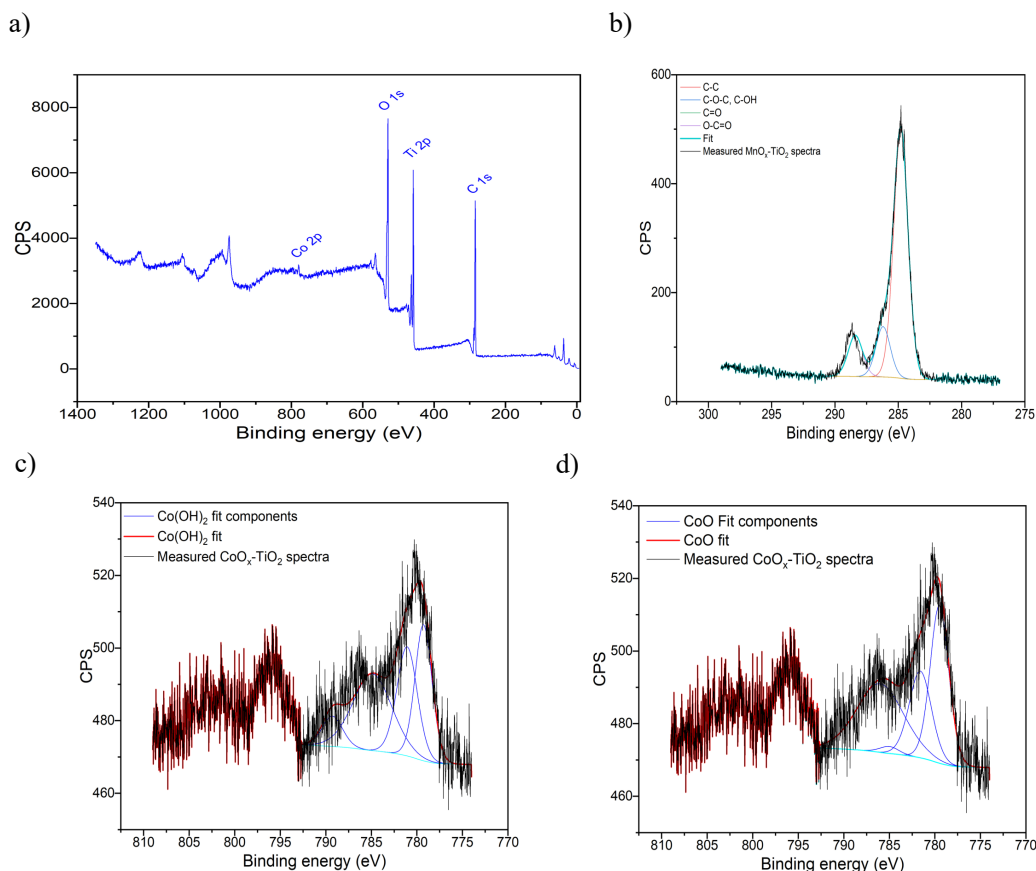


Figure 4.19: a) XPS survey spectrum of the $\text{CoO}_x\text{-TiO}_2$ treated at $350\text{ }^\circ\text{C}$ for 10 h. b) carbon spectra with the corresponding fit's. c) and d) Co in the sample with the corresponding Co(OH)_2 and CoO fit's.

dominant species in the composites. This again goes contrary to the products of pure precursor decomposition, where Co_3O_4 was generated. Interestingly, the used salt for the composite generation was a Co(III) salt, thus, a reduction of the Co^{3+} was taking place during the decomposition of the precursor. This, once again, can be caused by a radical formation during the decomposition of the salt, provoking such reduction.

The $\text{NiO}_x\text{-TiO}_2$ composite spectrum is shown in figure 4.20. Again, in a) the survey is shown and in c) the corresponding C 1s spectrum is presented. The signal corresponding to the Ni species has a low intensity, thus, it is difficult to extract accurate conclusion from the spectrum. In c) and d) are shown the corresponding Ni(OH)_2 and NiO fit for the recorded Ni species spectra. Comparison of the recorded data with the one from literature^{71,72} indicated that Ni(OH)_2 has the

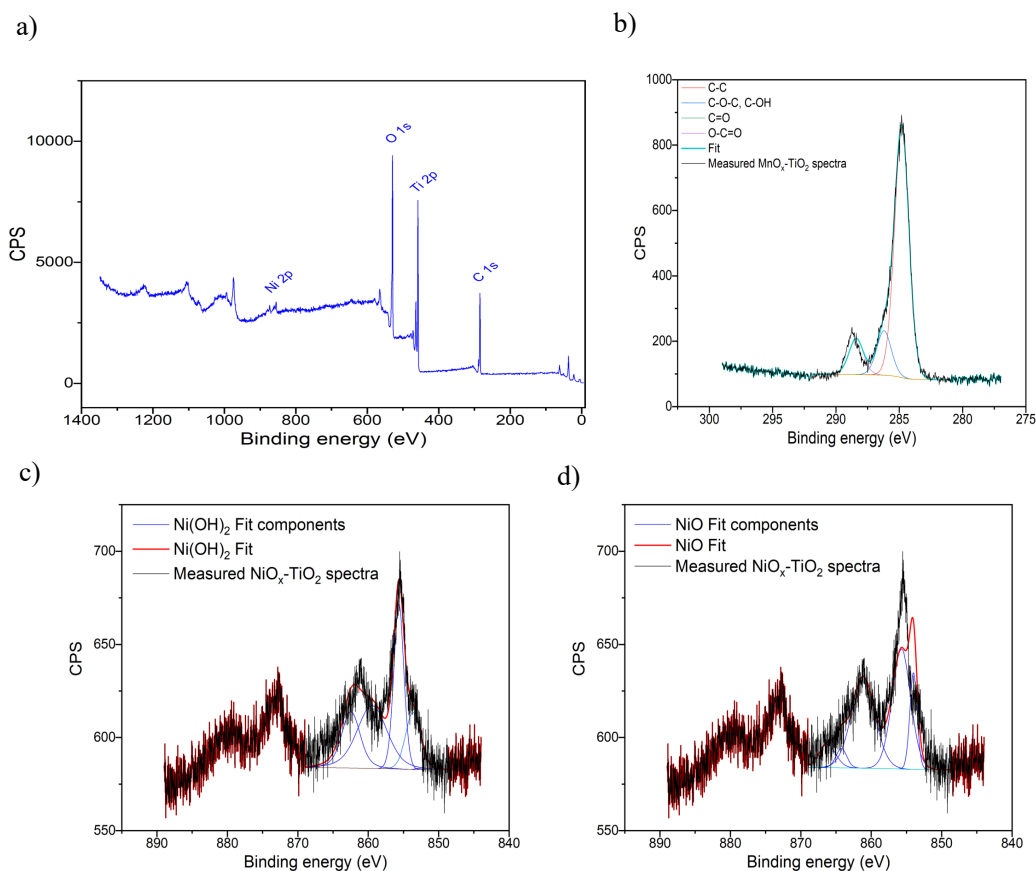


Figure 4.20: a) XPS survey spectrum of the $\text{NiO}_x\text{-TiO}_2$ treated at 350°C for 10 h. b) carbon spectra with the corresponding fit's. c) and d) Ni in the sample with the corresponding $\text{Ni}(\text{OH})_2$ and NiO fit's.

best fit, as shown in figure 4.20c and d. Although, the combination of $\text{Ni}(\text{OH})_2$, NiO and Ni reported by Biesinger et.al.⁷¹ revealed to have a similar profile. The spectrum obtained by them for the metallic Ni appears at lower binding energies. Thus, the combination of all three Ni species fits with the observed spectrum in our composite. Hence, it can be suggested that the composite contains metallic Ni and Ni(II). Interestingly, the formation of Ni was also observed for the pure precursor in the XRD in figure 4.3. Although, the Ni(II) was NiO, but not $\text{Ni}(\text{OH})_2$. Thus, again, it can be suggested another decomposition mechanism of the salt.

Figure 4.21 shows the spectrum for the $\text{FeO}_x\text{-TiO}_2$ sample with a) the survey and b) the C 1s spectra with the corresponding fit. In c) the corresponding Fe-species spectrum is shown. Again the signal to noise ratio is very small with additionally charging, complicating so complete evaluation. The recorded Fe-species

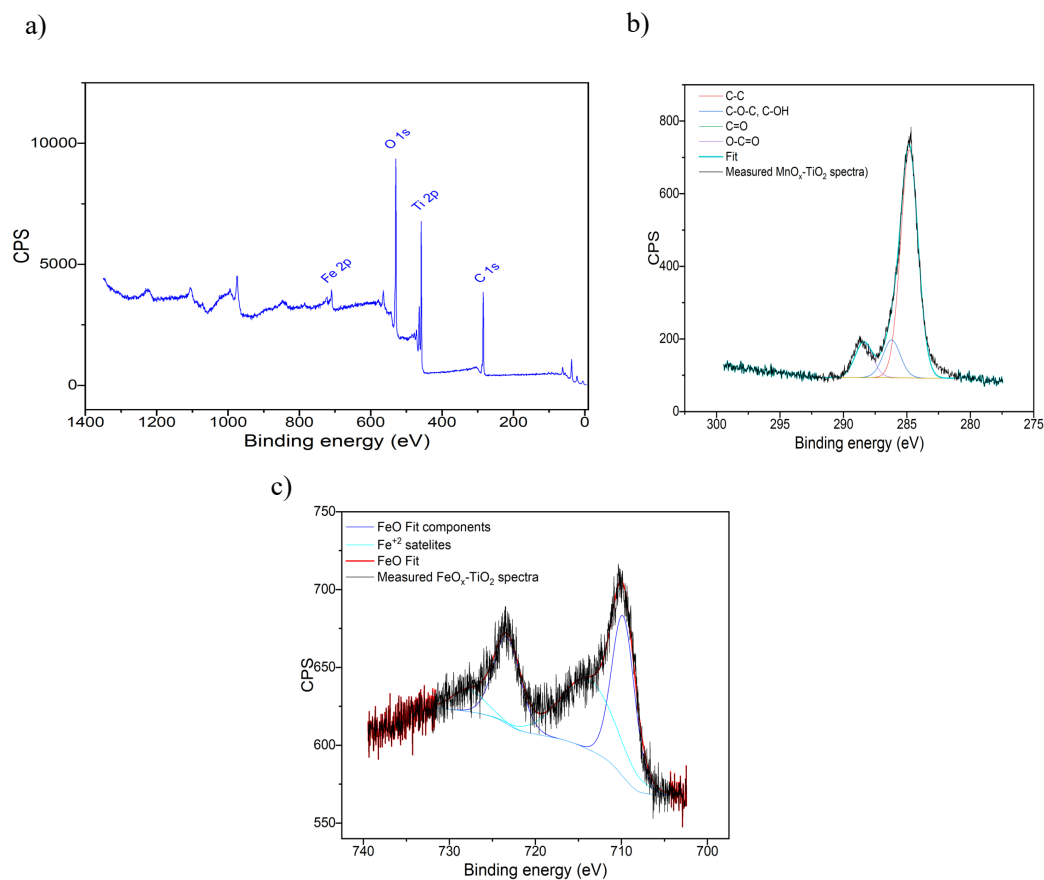


Figure 4.21: a) XPS survey spectrum of the $\text{FeO}_x\text{-TiO}_2$ treated at $350\text{ }^\circ\text{C}$ for 10 h. b) carbon spectra with the corresponding fit's. c) Fe in the sample with the FeO fit.

spectrum is shown with the corresponding FeO fit, showing the characteristic Fe(II) satellite at 714 eV. By comparison with literature^{70,73-75} it can be excluded the formation of Fe^{3+} species, like Fe_2O_3 , FeOOH and Fe_3O_4 . Even metallic Fe was possibly to exclude, as the signal appears at much lower binding energies and the characteristic spectrum is different than the one recorded for the composite. Thus, leading to the conclusion most probably FeO was generated. This is interesting as the used salt contains Fe(III) but not Fe(II). Thus, again a reduction took place. Which probably is the result of the intermediate decomposition products of the acetylacetonate. Again, for the pure precursor a Fe_3O_4 was observed (figure 4.3). Thus, only partial reduction took place, confirming again that the decomposition mechanism is different.

Figure 4.22 shows the $\text{CuO}_x\text{-TiO}_2$ composite with a) the survey and c) the C 1s. This sample shows strong charging, as observable in the C 1s spectrum with the

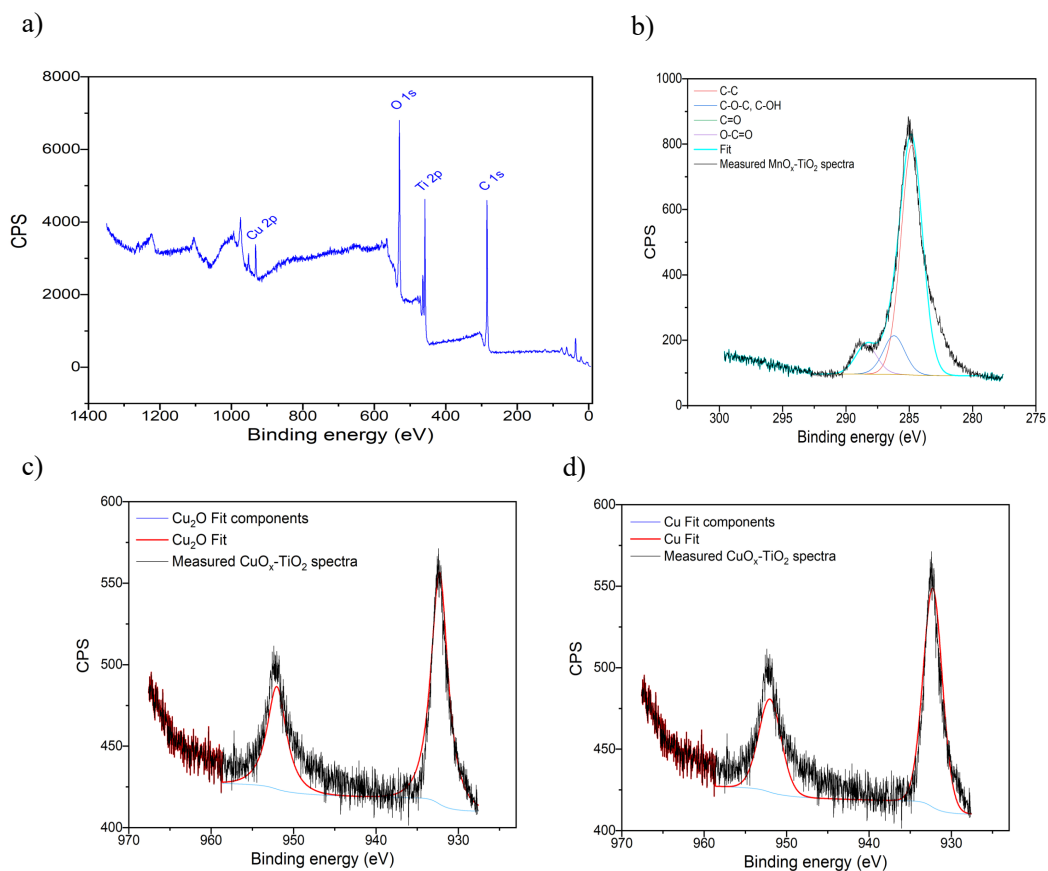


Figure 4.22: a) XPS survey spectrum of the $\text{CuO}_x\text{-TiO}_2$ treated at $350\text{ }^\circ\text{C}$ for 10 h. b) carbon spectra with the corresponding fit's. c) and d) Cu in the sample with the corresponding Cu_2O and metallic Cu fit's.

Lorentzian broadening. The detailed study of the Cu spectrum in c) and d) reveals that the best fitting compounds are Cu_2O and metallic Cu. Although, the reported weak signal satellite characteristic for Cu_2O is not visible here due to low signal to noise ratio.^{76,77} Thus, again this impedes clear interpretation. Nevertheless, it can be confirmed that no CuO and $\text{Cu}(\text{OH})_2$ is generated.⁷⁶ Thus, it can be suggested that metallic Cu and Cu(I) are the formed oxidation states on the composites. This fits well with the determined species for the precursor salt. There, it was seen that Cu, CuO and Cu_2O are generated. Hence, again reduction via radical formation takes place as the precursor salt contains Cu(II).

The XPS analysis of the composites revealed, again, that the oxides are difficult to characterize due to the low concentration of the attached oxides and additional charging of the sample. Thus, from the XPS data it was possible to extract

information about the possibly generated species.

4.3 Photocatalytic water splitting experiments

The synthesised composites were tested for the photocatalytic activity towards hydrogen evolution reaction (HER). The experimental procedure was designed in order to screen the activity of the obtained photocatalysts. To so first determine which composites are active photocatalysts. Longer tests are planned in the future for the active samples in order to extract stable evolution rates and investigate stability of the catalysts. Also to test the oxygen evolution reaction (OER) and the overall water splitting capacity of the composites.

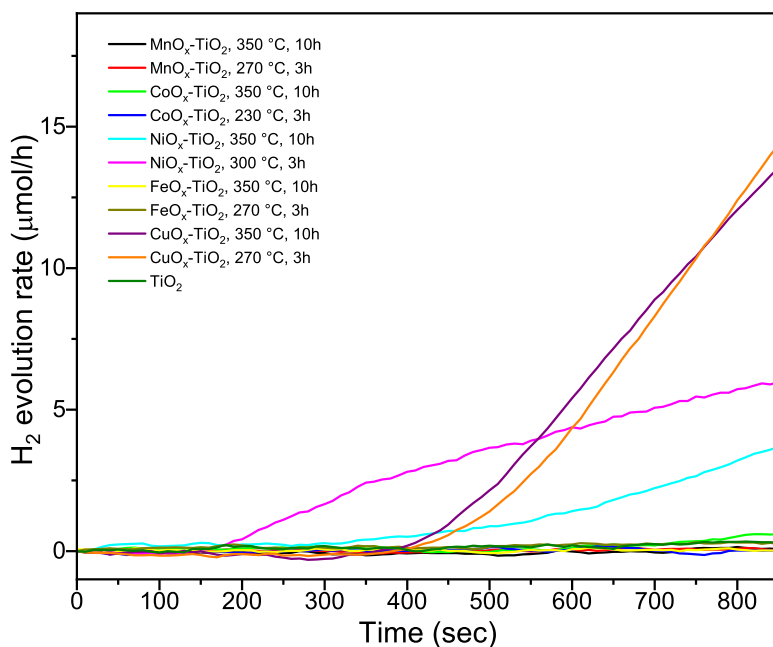


Figure 4.23: Graph representing the different water splitting photocatalytic activity of the metal oxide - TiO₂ composites at different temperatures and synthesised with the EtOH/Air method.

This HER activity test was done for all EtOH/Air synthesised MO_x-TiO₂ composites after two different thermal treatment programs for each composite (figure 4.23). The data shows that the MnO_x-TiO₂, CoO_x-TiO₂ and FeO_x-TiO₂

possess any photocatalytic activity towards HER, equal than the reference TiO_2 . While for $\text{NiO}_x\text{-TiO}_2$ and $\text{CuO}_x\text{-TiO}_2$ an enhanced photocatalytic activity is observable. However, for $\text{NiO}_x\text{-TiO}_2$ the different calcination programs showed different photocatalytic performance. With the one treated at $300\text{ }^\circ\text{C}$ for 3 h a higher H_2 evolution rate is observable than the one treated at $350\text{ }^\circ\text{C}$ for 10 h. Nevertheless, both have a similar slope at the end, which could suggest that the sample treated at $300\text{ }^\circ\text{C}$ just gets activated faster than the $350\text{ }^\circ\text{C}$ sample but may reach the same HER evolution rate maximum. Finally, $\text{CuO}_x\text{-TiO}_2$ samples showed much higher activity than $\text{NiO}_x\text{-TiO}_2$ and with no apparent differences between the various thermal treated samples. Interestingly, as can be seen in the plot, the $\text{CuO}_x\text{-TiO}_2$ evolution profiles have an activation delay of 200 seconds with regard to the $\text{NiO}_x\text{-TiO}_2$ samples, suggesting a different photocatalytic activation mechanism.

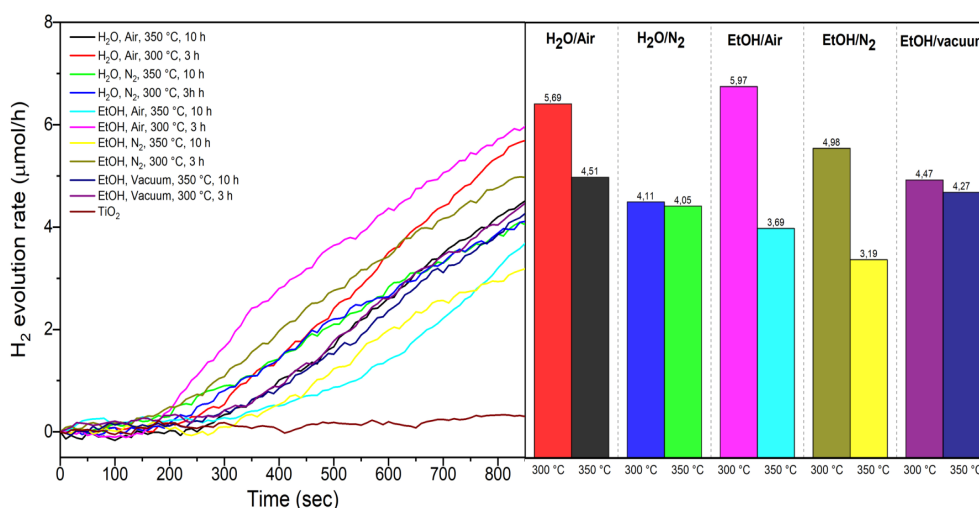


Figure 4.24: Graph to compare the different water splitting photocatalytic activity of the $\text{NiO}_x\text{-TiO}_2$ composites at different temperatures and synthesised by different methods. Left: H_2 evolution rate over time. Right: H_2 evolution rate at 850 seconds with the maximum rate measured shown on each column.

This differences in the behaviour can be related to the already discussed TGA data in section 4.2.2.2 and XPS in section 4.2.3. Based on the TGA data, we suggested that the $\text{MnO}_x\text{-TiO}_2$, $\text{CoO}_x\text{-TiO}_2$ and $\text{FeO}_x\text{-TiO}_2$ most of the decomposition products of the acetylacetonate remains adsorbed on the TiO_2 substrate after decomposition. These organic residues on the composite can act as a inhibitor, thus the nanoparticles are not HER active. For $\text{NiO}_x\text{-TiO}_2$ the tem-

peratures of 300 °C and 350 °C were used for the calcination. The mass loss TGA profile in figure 4.15 showed a step from 301 °C and ending at 366 °C which we suggested to correspond to the main acetylacetonate decomposition. Thus, the first chosen temperature is supposed to yield still a considerably amount of the acetylacetonate anion adsorbed on the TiO₂ substrate. The second temperature, on the other side, is supposed to yield much more of the nickel oxide. As the 300 °C sample is more active, the previous statement, with the acetylacetonates acting as inhibitor, is in contradiction with this observed behaviour. The XPS data from section 4.2.3 suggested that for the Mn, Co and Fe species only oxides were generated, while for Ni a metallic species was present, thus, the activity probably is related to the metal species present in the sample, and not the remnants of the acetylacetonate decomposition. For CuO_x-TiO₂ the last decomposition kink appears at 256 °C (figure 4.17). Meaning, that the used temperature, 270 °C and 350 °C, are both above this temperature. This, in turn, suggest the formation of similar oxides species in both cases as can be further confirmed by similar kinetics (initiation time) and slope (activity) of the HER profiles. The CuO_x-TiO₂ sample, similar to NiO_x-TiO₂, the XPS data also showed the same behaviour with the formation of a metallic species. Hence, it can be suggested that the different activity of the photocatalyst is due to the generated metallic species, as well as the morphology, as the TEM data in section 4.2.1 revealed that the Cu and Ni samples were coating the TiO₂, while the others not, thus more active sides.

As NiO_x-TiO₂ and CuO_x-TiO₂ showed to be photocatalytically active towards HER, all synthesised composites, prepared under H₂O/air, H₂O/N₂, EtOH/N₂ and EtOH/vacuum, were tested. In figure 4.24 HER profiles of all Ni synthesised composites treated at different temperatures are shown. Revealing that all NiO_x-TiO₂ samples are active. Interestingly, the data indicate that each sample treated at 300 °C show a higher activity than the corresponding sample treated at 350 °C. Suggesting that the active species is formed at 300 °C and get annihilated at higher temperatures. Thus, the chosen thermal treatment and the synthetic method indeed affect the photocatalytic activity. In section 4.2.1 TEM showed for CoO_x-TiO₂ and MnO_x-TiO₂ that slightly different synthetic methods induce changes in the morphology of the catalysts. These data from figure 4.24 certainly confirms that these different synthetic methods indeed induce differences in morphology and probably the generated metallic species, affecting so the photocatalytic activity. Unfortunately no TEM and XPS data are yet available for the other NiO_x-TiO₂ composites to visualize these differences, as only the EtOH/air sample TEM and XPS data are available.

In figure 4.25 it is shown the activity of all CuO_x-TiO₂ catalysts. Revealing that the sample with the highest activity are the one made in EtOH/vacuum with a H₂ evolution rate up to 56,2 μmol/h after 850 seconds. The one with

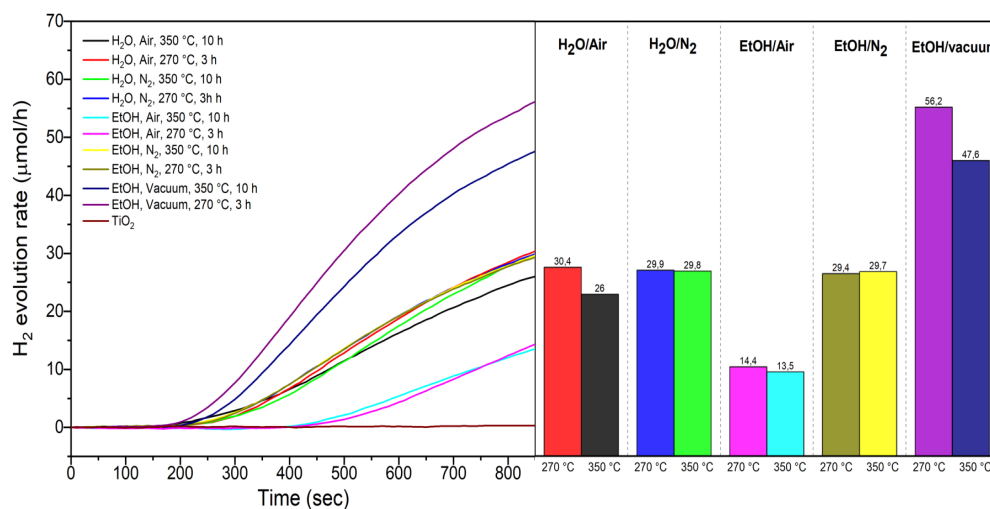


Figure 4.25: Graph to compare the different water splitting photocatalytic activity of the $\text{CuO}_x - \text{TiO}_2$ composites at different temperatures and synthesised by different methods. Left: H_2 evolution rate over time. Right: H_2 evolution rate at 850 seconds with the maximum rate measured shown on each column.

the lowest activity is the one synthesised in EtOH/air with a rate of just 13,5 $\mu\text{mol/h}$. Here the samples show that the different temperature does not affect so much the performance. This was expected, since the chosen thermal temperatures lie in the area where the CuO_x are already formed, thus, no difference expected. However, the EtOH/vacuum and $\text{H}_2\text{O}/\text{air}$ samples showed a stronger differences in the performance. With the composites treated at 270 °C more active than the one at 350 °C, thus the different synthesised samples have a different thermal behaviour, as probably different species and morphologies are generated on the TiO_2 . So, again, it is proved that the different synthesis affect the activity of the photocatalyst.

Conclusions

Photocatalysis is a promising way to overcome the challenge to generate and store clean and renewable energy. A photocatalyst has the capacity to convert and store light energy in a chemical bond, like in the case of H₂ generation through water splitting. But, the state-of-the-art energy conversion performance of the current photocatalysts is yet not efficient enough. One strategy to improve photocatalytic performance is to use the so called co-catalyst, which provide new catalytic active sites as well as enhance charge separation. But, the best co-catalyst up to day are based on noble metals that are rare and expensive, thus creating a drive to search for alternatives. We focused on Mn, Co, Ni, Fe and Cu to generate novel metal oxide co-catalyst for the photocatalytic improvement of TiO₂ for water splitting.

The goal of this thesis was to develop a new photocatalyst for H₂ generation by splitting water using light. For this, first a new approach for the synthesis of those photocatalyst needed to be developed. The used synthetic method (wet impregnation) consisted of TiO₂ nanoparticles impregnation (in form of commercial P25) with the corresponding metal salt (Mn(acac)₂, Co(acac)₃, Ni(acac)₂, Fe(acac)₃ and Cu(ac)₂) followed by thermal treatment to convert it into the corresponding oxide species. This impregnation was achieved by suspending TiO₂ and solubilizing the salt in EtOH or H₂O, depending on the synthetic method, and evaporating the solvent while stirring. This impregnation was carried out by using different synthetic environments (ambient atmosphere, N₂ atmosphere or vacuum), as some of the pure salts revealed instability in water based solutions. The developed synthetic methods induced different morphologies of the attached metal salts, and later oxides on TiO₂, as revealed by TEM for each five MnO_x-TiO₂ and CoO_x-TiO₂ samples. Also, TEM revealed that for some samples the attachment is not homogeneous. This differences were also observable without using electron microscopy, as the samples have different grain structures and colour intensities. Hence, the various synthetic approaches (and metals) induce different morphologies of the attached MO_x and adsorption strength of the salt on TiO₂ nanoparticles.

The thermal behaviour of the samples, investigated with TGA, revealed that the pure precursor salt and the salt/TiO₂ composites behave completely different.

The pure salts showed to be stable until a certain temperature range before the decomposition started and also after a stable oxide is formed at the end of calcination. The composites, on the other hand, show to continuously lose mass from room temperature, until the end of heating, 800 °C. There are two possible reasons for this behaviour: the presence of TiO₂ and/or the differences in the decomposition mechanism/products of the acetylacetonate anions. TiO₂ because the pure TiO₂ also shows this continued decrease in mass until 800 °C. The acetylacetonate anion because calculation indicated that a certain amount of the organic anion is still attached on the TiO₂, also at 800 °C. Thus, we believe the decomposition products of the acetylacetonates remain attached to the TiO₂ surface and continue to be decomposed, thus leading to the observed continuous mass loss until 800 °C.

The characterisation by using XRD and electron diffraction of the composites revealed that the MO_x nanoparticles attached on TiO₂ have an amorphous nature as only the two TiO₂ phases are visible, rutile and anatase. Thus, XPS was used to determine the chemical nature of the generated MO_x. But again this showed some impediment for the complete characterisation, as the metal content is very low and the samples are charging. The NiO_x-TiO₂ and CuO_x-TiO₂ samples showed that probably a mixture of metallic Ni, NiO, Ni(OH)₂ and metallic Cu, Cu₂O, respectively, are generated, thus, the synthetic parameters were not just limited in oxide generation. On the other hand, in MnO_x-TiO₂, CoO_x-TiO₂ and FeO_x-TiO₂ the produced species are MnO, Mn₂O₃, CoO, Co(OH)₂ and FeO, respectively. Thus, for Fe, Mn and Co the synthetic parameters ensured the formation of the oxides. Interestingly, a reduction of the oxidation state of the metals has taken place in all samples, probably driven through radical formation of the acetylacetonate anion decomposition products.

The particles were tested for the HER and revealed that NiO_x-TiO₂ and CuO_x-TiO₂ are active, while FeO_x-TiO₂, CoO_x-TiO₂ and MnO_x-TiO₂ are not. The different activity is probably induced by the presence of metallic Ni and Cu, species absent in the other samples, as well as the different morphology since NiO_x and CuO_x are coating the TiO₂ nanoparticles, providing more active sites. Furthermore, the different synthesis and heat treatment of the samples revealed to affect the HER performance. The NiO_x-TiO₂, EtOH-air sample heat treated at 300 °C for 3 h is the most active one. For the CuO_x-TiO₂ the EtOH-vacuum sample treated at 270 °C for 3 h showed the highest performance with respect to the other CuO_x-TiO₂ samples. Generally, all synthesised CuO_x-TiO₂ are more active than NiO_x-TiO₂. Another important observation is that the samples treated at higher temperature (350 °C) were less active than the samples calcinated at lower temperatures. This is probably because oxidation at higher temperatures of the reduced species is taking place and further decomposition of the acetylacetonate anion, thus the HER active species is probably annihilated at

higher temperatures.

Outlook

This thesis revealed that the synthesised nanoparticles are very difficult to characterise as many different methods have been used without complete success to fully reveal their composition and structure. For this reason further research with DRS spectroscopy, EELS and XAS as potential methods, is necessary on this system. Besides, more photocatalytic experiments to reveal maximum HER activity and stability as well as test the feasibility of water oxidation with the obtained photocatalysis will be of interest. The different heat treatment revealed to affect differently the performance of the samples, thus, further investigation to determine the optimal heat treatment/photocatalytic performance is necessary. Also the use of other salts, with other anions, as the decomposition mechanism will be different, to improve photocatalytic performance can be attempted. For further characterisation TEM images are necessary for all HER active species, to correlate morphology with activity. The synthetic method revealed to be not homogeneous for some samples, thus other methods to achieve more control should be investigated. Further, to make photocatalyst not just with one metal but with a mixture of different metals to determine possible synergistic effects can be of interest.

Acknowledgement

I want to thank to many people that helped me in my way to get where I am, so I will start with my boss, Dominik Eder who provided me the chance to work in his awesome group and on this super interesting topic. The other person that I want to greatly thank is my supervisor, Alexey Cherevan, for its really good supervision, for introducing and convincing me for this awesome topic, for giving me so much of his time for discussions and sharing his knowledge and experience to improve and rethink my data (also if sometimes at the beginning I was not agree). But, also for all the correction that he did in this thesis, helping me to improve my scientific writing. Also definitely I want to thank him to show me to get better organized, which I really needed. Thank you for all my improvement. The other persons that I would like to thank is Ariane Giesriegl (hopefully not written wrong this time) for all the TEM measurements done, as she did a lot! Also Tushar Gupta for the rest of the TEM measurement. To Greta Haselmann, for the XPS measurements performed and help in understanding and evaluate the data as also to teach me in better evaluate other data. Sreejith Nandan for the XRD measurements and showing me how to how to treat the diffractograms. To all this people I want to really thank for their help to accomplish this master thesis, which definitely without them would have not been possible, and also for their patient and willing to help when needed. But, of course also for the nice time spendend together after work and during work. Well, and I will not forget to thank our most loved, most appreciated and desired kika table, that refreshed our minds by hating and love each other (depending who was playing with who). Thank you for all the games and nice time spendend together. Well and of course I will not forget Uni Wien for forcing me to delete my front page and substitute it by this ugly one, thank you....

The other persons that I would like to thank in my development as a scientist are the supervisors that I had during my master study. I want to specially mention Prof. Wolfgang Kautek, for taking me to my first two conferences and bringing me to the dark side of physical chemistry. Also to ESG for paying for the conferences. And specially, Aida Naghilou, who I meet being my supervisor and evolved to a great friendship. I want to thank her because she was an important person in my scientific career, with discussions, showing me to think more scientifically and for

promoting me, thank you.

I want to thank my lovely brother, Desmond Schubert, who always supported and encouraged me on my path, and listened to me when I needed it. As also my father for all his economic help this years, helping me and making my path easier.

The last person I want to thank is the love of my life, Daniel Moseguí González, l'amor de la meva vida, que he tingut la sort de trobar i tenir amb mi cada dia quan em cal i ho necessito, t'estimo amor, per sempre estar allà i ferme créixer com a persona intel·lectual i emocional, m'ha tocat el gordo de la loteria! T'estimo infinit i espero compartir la resta de la meva vida amb tu i complir els nostres somnis junts. T'estimo cuseteta meva. Avui en dia estic on estic, gracies a tu també, T'estimo.

Curriculum Vitae

Persönliche Angaben

Name: Jasmin Sophia Schubert
Tel. Nr.: +43 677 618 328 43
E-Mail: jasmin.schubert2@gmail.com
Staatsangehörigkeit: Deutsch
Geburtsdatum: 10.04.1989

Ausbildung

10.2016 – Master Chemie
Universität Wien, Wien, Österreich

10.2015 – 07.2016 Erasmus Programm
Universität Wien, Wien, Österreich
Bachelorarbeit „Uranium extraction from aqueous solutions via ionic liquids“ (Institut für Umwelt und Radiochemie)

09.2011 – 07.2016 Bachelor Chemie
Universitat Autònoma de Barcelona (UAB), Barcelona, Spanien

09.2010 – 01.2011 Bachelor Umweltwissenschaften (Unabgeschlossen)
Universitat de Girona (UdG), Girona, Spanien

Arbeitserfahrung

02.2016 – Chemie Nachhilfe für Bachelor Studenten

08.2016 – 03.2017 Praktikum: Charakterisierung der Laser-Metall-Wechselwirkung mittels AFM, SEM und weitere Mikroskopietechniken
Institut für Physikalische Chemie, Universität Wien, Wien, Österreich

06.2014 - 08.2014 Laborpraktikantin an Organische Synthese von Photoschaltern
Ludwig Maximilian Universität (LMU), München, Deutschland

Publikationen und Tagungen

20.03 – 25.03.2017 Tagung „Nano and Photonics & FemtoMat 2017“ . Poster-Beitrag :
„Femtosecond laser generation of microbumps on stacked Cu/Ag thin films“
Institut für Physikalische Chemie, Universität Wien, Wien, Österreich

25.09 – 28.09.2017 Tagung „17.Österreichische Chemietage 2017“ . Poster-Beitrag :
„Femtosecond laser generation of microbumps on stacked Cu/Ag thin films“
Institut für Physikalische Chemie, Universität Wien, Wien, Österreich

Manuskript in Vorbereitung A. Naghilou, J. S. Schubert, Prof. W. Kautek, et. al. "Femtosecond laser generation of microbumps on stacked Cu/Ag thin films"
Institut für Physikalische Chemie, Universität Wien, Wien, Österreich

Sprachen und IT

Sprachkenntnisse:	Deutsch (Muttersprache) Spanisch (Muttersprache) Katalanisch (Muttersprache) Englisch (Verhandlungssicher) Französisch (Grundkenntnisse)
IT	Windows (OS), Office, Linux (OS), LaTeX, Chemdraw, Origin, Inkscape

Sonstiges

01.2017 –	Mitglied des Österreichischen Studienförderungswerk „Pro Scientia“
20.03 – 25.03.2017	ESG (Erwin Schrödinger Society) Stipendium
10.2015 – 07.2016	European Commission Erasmus+ Stipendium

References

- [1] NASA. Global climate change vital signs of the planet, April 2018.
- [2] IPCC. Ipcc fourth assessment report: Climate change 2007, April 2018.
- [3] International Energy Agency (iea). Global energy & co2 status report - the latest trends in energy and emissions in 2017, April 2018.
- [4] REN21. Renewables 2016 global status report, 2016.
- [5] UNDP, April 2018.
- [6] J.Perron H.Ibrahim, A.Ilinca. Energy storage systems—characteristics and comparisons. *Renewable and Sustainable Energy Reviews*, 2008.
- [7] Agata Godula-Jopek. *Hydrogen Production by Electrolysis*. Wiley-VCH Verlag GmbH & Co, 2015.
- [8] Mazlan Abdul Hosseini, Seyed Ehsan Wahid. Hydrogen production from renewable and sustainable energy resources: Promising green energy carrier for clean development. *Renewable and Sustainable Energy Reviews*, 2016.
- [9] Christopher L. Marshall Manuela Serban, Michele A. Lewis and Richard D. Doctor. Hydrogen production by direct contact pyrolysis of natural gas. *Energy & Fuels Advanced Search*, 2003.
- [10] Bruce E. Logan. Peer reviewed: Extracting hydrogen and electricity from renewable resources - a roadmap for establishing sustainable processes. *Environ. Sci. Technol.*, 2004.
- [11] Mohammad Mansoob Khan. *Nanocomposites for Visible Light-induced Photocatalysis*. Springer, 2017.
- [12] Rakshit Ameta and Suresh C. Ameta. *Photocatalysis - Principles and application*. Taylor & Francis Group, 2017.

-
- [13] Jinhua Ye Gianluca Li Puma Jenny Schneider, Detlef Bahnemann and Dionysios D. Dionysiou. *Photocatalysis: Fundamentals and Perspectives*. The Royal Society of Chemistry, 2016.
- [14] Junjie Chen. Homogeneous and heterogeneous catalysis:teachings of the thermal energy and power engineering course. *World Academy of Science, Engineering and Technology International Journal of Educational and Pedagogical Sciences*, 2014.
- [15] Shunichi Fukuzumi and Dachao Hong. Homogeneous versus heterogeneous catalysts in water oxidation. *Eur. J. Inorg. Chem.*, 2014.
- [16] Alex Omo Ibhaddon and Paul Fitzpatrick. Heterogeneous photocatalysis: Recent advances and applications. *Catalysts*, 2013.
- [17] Akihiko Kudo and Yugo Miseki. Heterogeneous photocatalyst materials for water splittingw. *Chemical Society Reviews*, 2008.
- [18] Pingwu Du Gengeng Luo Brian Lindley Theodore Lazarides, Theresa McCormick and Richard Eisenberg. Making hydrogen from water using a homogeneous system without noble metals. *JACS communications*, 2009.
- [19] Joshua D. Lawrence Frederic Gloaguen and Thomas B. Rauchfuss. Biomimetic hydrogen evolution catalyzed by an iron carbonyl thiolate. *J. Am. Chem. Soc.*, 2001.
- [20] Hyunwoong Park Soonhyun Kim and Wonyong Choi. Comparative study of homogeneous and heterogeneous photocatalytic redox reactions: Pw12o403-vs tio2. *J. Phys. Chem. B*, 2004.
- [21] Akihiko Kudo and Yugo Miseki. Heterogeneous photocatalyst materials for water splitting. *Chemical Society Reviews*, 2008.
- [22] Dennis Y.C. Leung K. Sumathy Meng Ni, Michael K.H. Leung. A review and recent developments in photocatalytic water-splitting using tio2 for hydrogen production. *Renewable & sustainable energy reviews*, 2007.
- [23] Alireza Shirazi Amin Ran Miao Wenqiao Song Tahereh Jafari, Ehsan Mohareri and Steven L. Suib. Photocatalytic water splitting—the untamed dream: A review of recent advances. *Molecules*, 2016.
- [24] Blok K Bode H Frenz W Gather C Hanekamp G Imboden D Jahnke M Kost M Kurz R Nutzinger HG Ziesemer T Steger U, Achterberg W. The average global rate of photosynthesis is 130 tw. *Sustainable development and innovation in the energy sector*, 2005.

- [25] Robert R. Crichton and Ricardo O. Louro. *Practical Approaches to Biological Inorganic Chemistry*. Elsevier, 2013.
- [26] Anthony F. Collings and Christa Critchley. *Artificial Photosynthesis*. 2005.
- [27] Murielle; Fontecave Marc; Artero Vincent Andreiadis, Eugen S.; Chavarot-Kerlidou. Artificial photosynthesis: From molecular catalysts for light-driven water splitting to photoelectrochemical cells. *Photochemistry and Photobiology*, 2011.
- [28] Kevin P Mendoza-Cortes, J. Lucht. Birnessite: A layered manganese oxide to capture sunlight for water-splitting catalysis. *J. Phys. Chem. C.*, 2016.
- [29] Andrea; Toma Francesca; Puntoriero Fausto; Scandola Franco; Campagna Sebastiano; Prato Maurizio; Bonchio Marcella Carraro, Mauro; Sartorel. Artificial photosynthesis challenges: Water oxidation at nanostructured interfaces. *Topics in Current Chemistry. Topics in Current Chemistry*, 2011.
- [30] Sakata T. Kawai T. Photocatalytic hydrogen production from liquid methanol and water. *J Chem Soc Chem Commun*, 1980.
- [31] Kawai T Sakata T. Heterogeneous photocatalytic production of hydrogen and methane fro methanol and water. *Chem Phys Lett*, 1981.
- [32] Disdier J Courbon H Mozzanega MN Pichat P, Herrmann JM. Photocatalytic hydrogen production fro maliphatic alcohols over a bifunctional platinum on titanium dioxide catalyst. *Nouv J Chi m*, 1981.
- [33] Susumu Yoshikawa Thammanoon Sreethawong, Yoshikazu Suzuki. Photocatalytic evolution of hydrogen over mesoporous tio2 supported nio photocatalyst prepared by single-stepsol-gel process with surfactant template. *International Journal of Hydrogen Energ*, 2005.
- [34] Ken-ichi MARUYA Akihiko KUDO, Kazunari DOMEN and Takaharu ONISHI. Photocatalytic activities of tioa loaded with nio. *CHEMICAL PHYSICS LETTERS*, 1987.
- [35] Qin-Dong Huang Mei-Ting Fan You-Zhu Yuan Timothy Thatt-Yang Tan Dai-Wei Liao Jing-Dong Lin, Shi Yan. Tio2 promoted by two different non-noble metal cocatalysts for enhanced photocatalytic h2 evolution. *Applied Surface Science*, 2014.
- [36] Yanyu Zhang-Hongxing Jia Zijun Sun Pingwu Du Zhiping Yan, Xingxing Yu. Enhanced visible light-driven hydrogen production from water by a noble-metal-free system containing organic dye-sensitized titanium dioxide loaded

- with nickel hydroxide as the cocatalyst. *Applied Catalysis B: Environmental*, 2014.
- [37] Yang Hai Jiaguo Yu and Bei Cheng. Enhanced photocatalytic h₂-production activity of tio₂ by ni(oh)₂ cluster modification. *J.Phys.Chem.C*, 2001.
- [38] Sudip K. Batabyal Lydia H. Wong James Barberand Joachim Say Chye Loo hong D. Tran, Lifei Xi. Enhancing the photocatalytic efficiency of tio₂ nanopowders for h₂ production by using non-noble transition metal co-catalysts. *Phys. Chem. Chem. Phys*, 2012.
- [39] Yu Wang Lingbin Zhu Xiaohong Xia Zhongbing Huang Jingjing Si, Shuying Xiao and Yun Gao. Sub-nanometer co₃o₄ clusters anchored on tio₂(b) nano-sheets: Pt replaceable co-catalystsfor h₂ evolution. *Royal society of chemistry*, 2018.
- [40] Nishijima Hiroaki Yamamoto Hironori Fujishima Musashi Okuoka Shin ichi Hattori Takanori Sumida Yasutaka Kobayashi Hisayoshi Tada Hiroaki, Jin Qiliang. Titanium(iv) dioxide surface modified with iron oxide as a visible light photocatalyst. *Angewandte Chemie International Edition*, 2011.
- [41] Huogen Yu, Hiroshi Irie, Yoshiki Shimodaira, Yasuhiro Hosogi, Yasushi Kuroda, Masahiro Miyauchi, and Kazuhito Hashimoto. An efficient visible-light-sensitive fe(iii)-grafted tio₂ photocatalyst. *The Journal of Physical Chemistry C*, 2010.
- [42] Min Liu, Xiaoqing Qiu, Masahiro Miyauchi, and Kazuhito Hashimoto. Cu(ii) oxide amorphous nanoclusters grafted ti³⁺ self-doped tio₂: An efficient visible light photocatalyst. *Chemistry of Materials*, 2011.
- [43] Zhikang He, Junwei Fu, Bei Cheng, Jiaguo Yu, and Shaowen Cao. Cu₂(oh)₂co₃ clusters: Novel noble-metal-free cocatalysts for efficient photocatalytic hydrogen production from water splitting. *Applied Catalysis B: Environmental*, 2017.
- [44] J. Bandara, C. P. K. Udawatta, and C. S. K. Rajapakse. Highly stable cuo incorporated tio₂ catalyst for photocatalytic hydrogen production from h₂o. *Photochem. Photobiol. Sci.*, 2005.
- [45] Jiaguo Yu, Yang Hai, and Mietek Jaroniec. Photocatalytic hydrogen production over cuo-modified titania. *Journal of Colloid and Interface Science*, 2011.

- [46] Ang Li, Tuo Wang, Xiaoxia Chang, Weiting Cai, Peng Zhang, Jijie Zhang, and Jinlong Gong. Spatial separation of oxidation and reduction co-catalysts for efficient charge separation: Pt@tio₂@mnox hollow spheres for photocatalytic reactions. *Chem. Sci.*, 2016.
- [47] Xin Li, Jiaguo Yu, Jingxiang Low, Yueping Fang, Jing Xiao, and Xiaobo Chen. Engineering heterogeneous semiconductors for solar water splitting. *J. Mater. Chem. A*, 2015.
- [48] Bryan M. Hunter, Harry B. Gray, and Astrid M. Müller. Earth-abundant heterogeneous water oxidation catalysts. *Chemical Reviews*, 2016.
- [49] Alireza Shirazi Amin Ran Miao Wenqiao Song Tahereh Jafari, Ehsan Mohareri and Steven L. Suib. Photocatalytic water splitting-the untamed dream: A review of recent advances. *molecules*, 2016.
- [50] Daisuke Fujita Elisabeth Mansfield, Debra L. Kaiser and Marcel Van de Vorde. *Metrology and Standardization for Nanotechnology*. Wiley-VCH, 2017.
- [51] T. Alan Hatton R. Nagarajan, editor. *Nanoparticles: Synthesis, Stabilization, Passivation, and Functionalization*. American Chemical Society, Washington, DC, 2008.
- [52] Claudia Altavilla and Enrico Ciliberto, editors. *Inorganic Nanoparticles - synthesis, application and perspective*. CRC Press, 2011.
- [53] A. K. Cheetham C. N. R. Rao, A. Müller, editor. *The Chemistry of Nanomaterials - Synthesis, Properties and Applications*. WILEY-VCH, 2004.
- [54] C. Suryanarayana and M. Grant Norton. *X-Ray Diffraction. A Practical Approach*. 1998.
- [55] Paul Van Der Heide. *X-RAY PHOTOELECTRON SPECTROSCOPY-An Introduction to Principles and Practices*. 2012.
- [56] John Humphreys Peter J. Goodhew and Richard Beanland. *ELECTRON MICROSCOPY AND ANALYSIS*. 2001.
- [57] David B. Williams and C. Barry Carter. *Transmission Electron Microscopy-A Textbook for Materials Science*. 2009.
- [58] Barbara H. Stuart. *Infrared Spectroscopy: Fundamentals and Applications*. 2004.
- [59] PerkinElmer. *FT-IR Spectroscopy Attenuated Total Reflectance (ATR)*.

-
- [60] Paul Gabbott. *Principles and Applications of Thermal Analysis*. Blackwell Publishing, 2008.
- [61] Ulrike Diebold. The surface science of titanium dioxide. *Surface science reports*, 2003.
- [62] Ji Chul Jung Zailei Zhang and Ning Yan. Designed synthesis of mox (m = zn, fe, sn, ni, mn,co, ce, mg, ag), pt, and au nanoparticles supported on hierarchical cuo hollow structures. *The Royal Society of Chemistry*, 2016.
- [63] E. A. Anumol Paromita Kundu and N. Ravishankar. Pristine nanomaterials: synthesis, stability and applications. *The Royal Society of Chemistry*, 2013.
- [64] Lionel Vayssieres. Designing ordered nanoarrays from aqueous solutions. *Advanced Materials*, 2006.
- [65] Donglin Han Zhenkun Lin and Shufen Li. Study on thermal decomposition of copper(ii) acetate monohydrate in air. *J Therm Anal Calorim*, 2012.
- [66] Yasuhiro Yamada and Yoshihiko Kanemitsu. Determination of electron and hole lifetimes of rutile and anatase tio₂ single crystals. *APPLIED PHYSICS LETTERS*, 2012.
- [67] Junguang Tao Alan Kramer Eli Sutter & Matthias Batzill Tim Luttrell, Sandamali Halpegamage. Why is anatase a better photocatalyst than rutile? - model studies on epitaxial tio₂ films. *scientific reports*, 2014.
- [68] Dorian A. H. Hanaor and Charles C. Sorrell. Review of the anatase to rutile phase transformation. *J Mater Sci*, 2011.
- [69] Paul Gabbott. *Principles and Applications of Thermal Analysis*. Blackwell Publishing Ltd, 2008.
- [70] Andrew P. Grosvenor Leo W.M. Laua Andrea R. Gerson Mark C. Biesinger, Brad P. Payne and Roger St.C. Smart. Resolving surface chemical states in xps analysis of first row transition metals, oxides and hydroxides: Cr, mn, fe, co and ni. *Applied Surface Science*, 2011.
- [71] Leo W. M. Lau Andrea Gerson Mark C. Biesinger, Brad P. Payne and Roger St. C. Smart. X-ray photoelectron spectroscopic chemical state quantification of mixed nickel metal, oxide and hydroxide systems. *Surface and interface analysis*, 2009.

References

- [72] Roger St.C. Smart N. Stewart McIntyre Andrew P. Grosvenor, Mark C. Biesinger. New interpretations of xps spectra of nickel metal and oxides. *Surface science*, 2006.
- [73] Peter Hayes Toru Yamashita. Analysis of xps spectra of fe²⁺ and fe³⁺ ions in oxide materials. *Applied Surface Scienc*, 2008.
- [74] M. C. Biesinger A. P. Grosvenor, B. A. Kobe and N. S. McIntyre. Investigation of multiplet splitting of fe 2p xps spectra and bonding in iron compounds. *SURFACE AND INTERFACE ANALYSIS*, 2004.
- [75] M.P. Asta R. Pérez-López G. Román-Ross V. Illera J. Cama M. Cotte R. Tucoulou. Analysis of the iron coatings formed during marcasite and arsenopyrite oxidation at neutral-alkaline conditions. *G e o l o g i c a A c t a*, 2013.
- [76] Andrea R. Gerson Roger St.C. Smart Mark C. Biesinger, Leo W.M. Lau. Resolving surface chemical states in xps analysis of first row transition metals, oxides and hydroxides: Sc, ti, v, cu and zn. *Applied Surface Science*, 2010.
- [77] www.xpssimplified.com. Copper • transition metal, 2018.